EXPERIMENTAL SIMULATION OF THE HYDRODYNAMICS OF DISSIMILAR SOLIDS IN A PRESSURIZED CIRCULATING FLUIDIZED BED

by

Richard Hing-Fung Tan

B.S.M.E., State University of New York at Stony Brook (1995)

Submitted to the Department of
Mechanical Engineering
in Partial Fulfillment of the Requirements
for the Degree of

Master of Science in Mechanical Engineering

at the

Massachusetts Institute of Technology

June 1997

Signature of Author .....
Department of Mechanical Engineering
May 23, 1997

Certified by .....
Leon R. Glicksman
Professor, Department of Mechanical Engineering
Thesis Supervisor

Accepted by .....
Ain A. Sonin
Chairman, Department Committee on Graduate Studies
Department of Mechanical Engineering

Blank Page

EXPERIMENTAL SIMULATION OF THE HYDRODYNAMICS OF DISSIMILAR SOLIDS IN A PRESSURIZED CIRCULATING FLUIDIZED BED

by

Richard Hing-Fung Tan

Submitted to the Department of Mechanical Engineering
on May 23, 1997 in Partial Fulfillment of
the Requirements for the Degree of Master of Science in
Mechanical Engineering

ABSTRACT

The mixing and segregation of dissimilar solid particles of different densities and Particle Size Distributions (PSD) in a Pressurized Circulating Fluidized Bed (PCFB) riser are of primary interest. A commercial pyrolyzer which consists of limestone and char is a PCFB and can be properly designed to maximize, say reaction rate if the mixing and segregation processes are clearly understood.

By utilizing a lab-scale fluidized bed model with a properly selected solid to gas density ratio, the behavior of dissimilar solids in a pyrolyzer were simulated experimentally with different solid recirculation rates at a given superficial gas velocities. Volumetric solid fraction along the riser was measured in each case. Several sampling devices installed axially along the riser enabled the collection of solid bed particles at various levels. These samples were analyzed for both the PSD and material concentrations. Results indicated that at the current operating conditions and riser geometry, both the coarse and the fine were well-mixed within the riser. The presence of inertial separation near the top of the riser resulted in low coarse particle entrainment. Finer particles were less susceptible to inertial separation, resulting in a higher entrainment rate.

Thesis Supervisor: Leon R. Glicksman
Title: Professor of Architecture and Mechanical Engineering

Blank Page

ACKNOWLEGEMENTS

First of all, I would like to express my gratitude to my thesis advisor Professor Leon Glicksman for making my education here in MIT possible. His constant intellectual guidance and encouragement has helped and inspired me to improve the quality of this work. I also want to thank him for giving me the freedom and flexibility to take charge of the work while providing constant advice. He has enhanced my learning experience and made it an enjoyable one.

I would like to thank Mr. Mark Torpey from Foster Wheeler Development Corporation (FWDC) in Livingston, New Jersey for providing all essential pilot plant information necessary for the scope of this work. I sincerely hope this work will provide him and FWDC with some useful information.

Being able to work with some of the most outstanding graduate students in MIT has been my privilege. Special thanks goes to Peter Noymer and Paul Farrell who are both my peers and role models for performing research especially in fluidization. Their companionship has enhanced my educational experience in MIT.

I would also like to thank my parents and siblings for giving me the freedom to focus on my graduate education without demanding much in return. Special thanks goes to Frances with whom I have shared many ups and downs throughout the course of this work. This work is made possible by their unselfish love and constant encouragement.

Finally, I would like to acknowledge the generous financial support from the U.S. Department of Energy, Federal Energy Technology Center in Pittsburgh (Grant No. DE-FG22-95PC95228).

Blank Page

TABLE OF CONTENTS

LIST OF FIGURES

LIST OF TABLES

NOMENCLATURE

A_j	cross section area of jet/distributor
$\overline{C}_{coarse}$	volumetric fraction of coarse (plastic)
C_d	particle drag coefficient
CFB	circulating fluidized bed
ΔP	pressure drop, as measured by differential pressure transducer
d_p, $\overline{d_p}$	mean particle diameter
D	riser diameter
G_s	solid recirculation rate [kg/m^2s]
h	distance between two pressure taps
HIPPS	High Performance Power Systems
$\dot{m}$	mass flow rate of air of distributor
$m_{particle}$	mass of particle in a control volume
PCFB	pressurized circulating fluidized bed
PSD	particle size distribution
Q_{probe}	volumetric flow rate at a sample probe
u_{mf}, U_{mf}	minimum fluidization velocity
u_o, U_o	superficial gas velocity
u_t, U_t	particle terminal velocity
V_j	exit velocity of jet/distributor
V_{cork}	true volume of cork
$V_{plastic}$	true volume of plastic
x_c	mass fraction of cork
x_p	mass fraction of plastic

Greek Symbols

ε	particle void fraction
μ_f	kinematic viscosity of air
$\rho_{bulk\|c}$	cork bulk density
$\rho_{bulk\|mix}$	solid mixture bulk density
$\rho_{bulk\|p}$	plastic bulk density
ρ_s	solid density
$\rho_{s,\,local}$	local solid density
ρ_f	gas density
ϕ, Φ	sphericity

1. Introduction

1.1 Background

1.1.1 Fluidized Bed and its Features

A fluidized bed is a device in which fine solid particles are allowed to interact with a fluid so that chemical reactions can take place between the two phases and thermal energy exchange can take place between the two phases and the wall. Due to the uniform mixing property provided by a fluidized bed, the technology is used whenever good two-phase interactions are required.

The gas phase moves vertically upward through a bed of particles. The gas velocity is adjusted to achieve the desired regime of fluidization. The phenomenon of fluidization has been described by various authors in detail. Two of such literature are written by Kunii and Levenspiel (1969) and by Davidson, Clift and Harrison (1985). At a low gas flow rate where the gas velocity is less than the minimum fluidization velocity, solid particles barely move about their original position. This is a fixed bed. At a higher gas flow rate in which all particles in the system can be suspended by the upward flowing gas, the minimum fluidization velocity has been reached. This is a bed at minimum fluidization. At a still higher velocity not exceeding the particle terminal velocity, bubbles are formed as the higher volumetric flow rate of gas introduced into the system produces voids within the particles to escape. This condition is known as bubbling fluidization. Almost all particles being fluidized in this regime are not entrained but stay near the bottom of the bed. At a gas flow rate exceeding the particle terminal velocity, solid particles are now entrained by the fluidizing gas and leave the riser to be returned through a return leg. Particles "circulate" between the riser and the return leg; this is the Circulating regime. Finally a pneumatic transport regime is formed when the flow rate is very high relative to the particle terminal velocity. Almost complete entrainment results and solid particles can be depleted if they are not replenished by continuous recirculation.

A Circulating Fluidized Bed (CFB) can be used as a fossil fuel combustor in which coal, being the solid phase, is burned to produce thermal energy. Solid limestone particles are often used as a sorbent to remove sulfur from high-sulfur-content coal and to prevent the formation of gaseous pollutant sulfur dioxide (SO_2). The thermal energy produced in the combustor can be exchanged through heat exchangers and pipes near the CFB wall to produce steam which in turn can be used to drive a steam turbine for power generation. This steam cycle is the standard Rankine Cycle.

The very special features and characteristics of a fluidized bed bring about many advantages. Due to the high sulfur content in most coal, its combustion can result in the formation of gaseous SO_2. SO_2 is water soluble and thus dissolves in water to form acid rain. Through the use of limestone, sulfur can be captured to form a harmless solid sulfate (calcium sulfate) which can be drained from the combustor and discarded. The excellent mixing provided by the fluidized bed allows good contact and thus mixing between the sorbent and the coal. It minimizes the amount of harmful SO_2 released to the atmosphere. High combustion efficiency can also be achieved by the excellent gas-solid contact within the combustor. In a CFB, any unburned solid fuel (either coal or char) that escapes the riser can be captured and reinjected for further and complete oxidation. Lastly, high heat transfer rate can be obtained between the wall heat exchanger and the bed materials, allowing combustors with relatively small heat exchange surface area to achieve a satisfactory level of heat transfer.

Major components of a fluidized bed include a riser section in which combustion and heat exchange take place; a cyclone which is a gas-solid separator (whose entrance is connected to the riser exit); a return leg that recirculates entrained solids back into the riser; and a distributor in which fluidizing gas is injected. The coal and limestone are brought into the bed through feed systems which are sometimes integrated into the distributor design. In some design a valve is used to control the rate of solid reinjection from the return leg to the riser. The major components of a CFB are shown in Figure 1-1

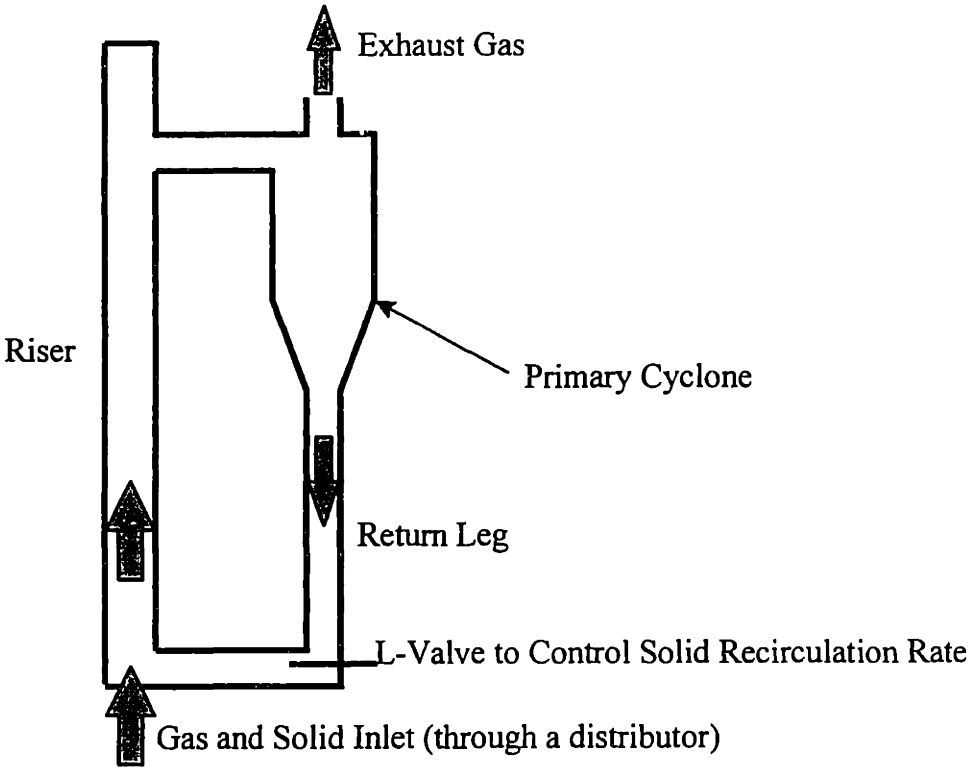

Figure 1-1 Major Components of a Circulating Fluidized Bed

1.1.2 Pyrolyzer and The Combined Cycle

A Pressurized Circulating Fluidized Bed (PCFB) is a CFB operating at an elevated pressure which can be anywhere from 10 atm to 20 atm. With the operation of a PCFB combustor, a combined-cycle configuration with a higher cycle efficiency is made possible. An atmospheric CFB combustor provides the thermal energy necessary to generate steam to drive a steam turbine. This is known as the Rankine cycle. The compressed air in a PCFB has high enthalpy from the elevated pressure and temperature and from either the partial combustion or complete combustion of coal within the bed. Work can be extracted from this high-enthalpy compressed air by routing it to a gas turbine and allowing expansion to take place. This is an open Brayton Cycle. The combined cycle, which consists of an open Brayton and a closed Rankine Cycle can increase the overall cycle efficiency to approximately 47%[1] from the current conventional single-cycle mid-thirty percent.

A combined-cycle High Performance Power System (HIPPS) has been proposed and designed by Foster Wheeler Development Corp. whereby coal is the only fuel used in the process. A pyrolyzer which is a PCFB, converts coal feed into a low-Btu fuel gas and char at an elevated pressure (240 psia) and temperature (1700°F). Input to the pyrolyzer also includes sorbent and air. As explained in the previous section, the sorbent is used for the absorption and capture of sulfur in the coal. The pyrolyzer operates at substoichiometric conditions so that both fuel gas and char produced can be oxidized further in their respective cycles. The fuel gas is separated from the char by a cyclone upon exiting the pyrolyzer. The char is transported to a combustor as a partially oxidized fuel for the Rankine Cycle while the fuel gas goes to a gas turbine as a combustible fuel for the Brayton Cycle. A process flow diagram illustrates the various components and the cycles discussed above.(Figure 1-2)

---

[1] Overall cycle efficiency suggested by Foster Wheeler Development Corp. (Livingston, New Jersey) in their High Performance Power System (HIPPS) report.

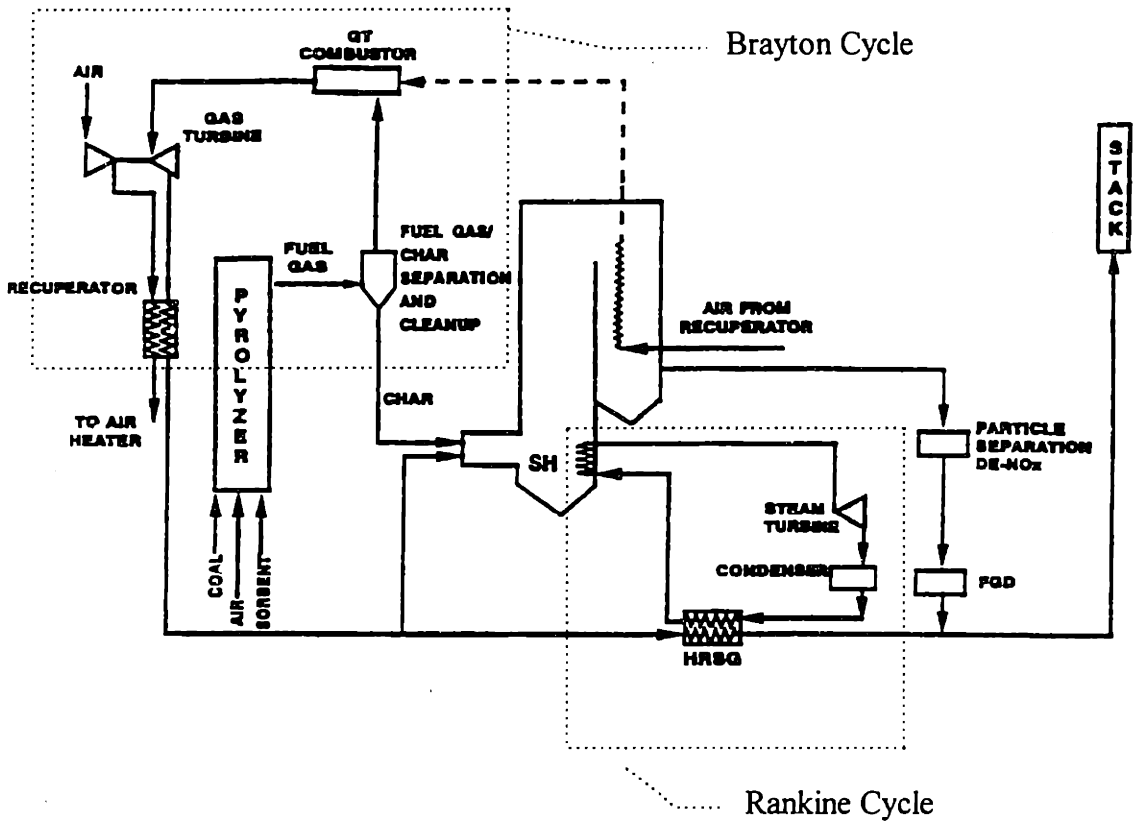

Figure 1-2 Simplified HIPPS Process Flow Diagram[2]

[2] Property of FWDC. Extracted from "Development of a high-performance coal-fired power generating system with pyrolysis gas and char-fired high temperature furnace" final report prepared for PETC, Pittsburgh, PA. Explanations for acronyms in the figure: HRSG - Heat Pecovery Steam Generator.

1.2 Hydrodynamic Scaling Laws

A lab scale cold model is a useful tool in simulating the hydrodynamics of a pilot plant or an actual system. Since the scaled cold model operates at atmospheric pressure and temperature, studies can be performed more at ease and more cost-effectively. However, there must be a set of scaling parameters that govern the hydrodynamic similarity between the model and the actual system; very much like the study of the drag and lift of a model airplane in a wind tunnel. This section briefly summarizes the procedures involved in the development of the scaling laws for both atmospheric and pressurized fluidized beds. Details related to this work can be found in Glicksman (1984) and Glicksman *et al* (1993, 1994). A more easily understandable approach to the derivation of the scaling laws can be found in Farrell (Chapter 2, 1996).

Dimensional Analysis is employed to understand the hydrodynamics of a fluidized bed. Both independent and dependent parameters that have an influence in the hydrodynamics of a fluidized bed are listed. Using Buckingham Pi Theorem, these parameters are non-dimensionalized by the independent parameters, resulting in the dimensionless Pi groups. Alternatively, the equations and boundary conditions governing the two-phase flow dynamics of a fluidized bed can be non-dimensionalized. (Glicksman (1984)). Independent dimensionless parameters similar to the Pi groups are formed. The results are a set of parameters that govern the scaling and modeling of a fluidized bed, known as the Full Set of Scaling Parameters:

$$\frac{\rho_s}{\rho_f} \quad \frac{u_o^2}{gD} \quad \frac{\rho_f u_o D}{\mu_f} \quad \frac{\rho_f u_o d_p}{\mu_f} \quad \frac{L}{D} \quad \frac{G_s}{\rho_s u_o} \quad \phi_s \quad PSD$$

The full set of scaling parameters once employed, determines the linear dimension L of the model for a given fluidizing gas. A pressurized fluidized bed operates anywhere between 10 - 20 atm. In order to simulate the hydrodynamics of a pressurized fluidized bed by using a scale model with air at atmospheric pressure and temperature, a model of approximately the same linear dimensions as the hot bed must be built according to the full set of scaling parameters. Thus making a cold model study impractical.

By expressing the Ergun drag equation in terms of minimum fluidization velocity u_{mf} and looking at the gas-particle drag at both the viscous and the inertia limit, modifications of the full set of scaling parameters can be simplified as followed:(Glicksman *et al.* (1993))

$$\frac{\rho_s}{\rho_f} \quad \frac{u_o^2}{gD} \quad \frac{u_o}{u_{mf}} \quad \frac{L}{D} \quad \frac{G_s}{\rho_s u_o} \quad \phi_s \quad PSD$$

This is known as the Simplified Set of Scaling Laws. The elimination of the bed and the particle Reynold's number from the full set of scaling laws allows the scale factor or linear dimensions to be specified independently, making the scaling of pressurized fluidized bed feasible. The scaling for this thesis work is based on the simplified set of scaling laws.

Although the simplified set of scaling laws are satisfied only exactly at high and low Reynold's number corresponding to the inertia and viscous regime respectively, intermediate regime can be approximated with reasonable accuracy. Errors in this intermediate regime has been quantified and presented by Farrell (Section 2.3.4.3 1996).

1.3 Objective and Motivation of Thesis Work

Coal is a low cost fossil fuel found abundantly in the U.S. However, improper combustion of coal will result in the emission of environmentally hazardous gases such as NO_x and SO_2 both of which are major contributions to acid rain. Thus there is an incentive to utilize the abundant coal reserves in a way acceptable to the environment.

Pressurized Fluidization is a technology that burns coal in a clean and efficient manner while simultaneously improving the overall cycle efficiency. Due to the effective mixing property of a fluidized bed, operation temperature can be lowered to reduce the formation of NO_x while sorbent can be introduced to remove sulfur from the coal. In addition, the cycle efficiency is increased with an elevated operating pressure. However,

commercialization of the technology and large scale construction of commercial units face uncertainties in scaling up from pilot plants. By utilizing the simplified scaling laws for Pressurized Fluidized Bed developed by Glicksman (1993) which has been verified for both pressurized circulating and pressurized bubbling fluidized bed by Glicksman *et al* (1995), good approximations of the hydrodynamics of a large scale commercial unit can be reproduced in a lab scale cold model. Therefore, a lab scale cold model is an ideal tool in helping the effort in the scale up and the commercialization of the Pressurized Fluidization technology.

The objective of this thesis work is to perform experimental simulations of the hydrodynamics of the pyrolyzer in a lab scale cold model. (it is a PCFB as discussed in section 1.1.2) The pyrolyzer is part of the HIPPS[3] project proposed and designed by FWDC[4]. The hydrodynamics of a fluidized bed affect the performance of the system and is thus an extremely important aspect to be studied. The simplified set of scaling law dictates the operating conditions and material properties between the pyrolyzer and the cold model. For the scope of this thesis work, the pyrolyzer is of primary interest. (Figure 1-3)

[3] High Performance Power Systems
[4] Foster Wheeler Development Corporation (Livingston, New Jersey)

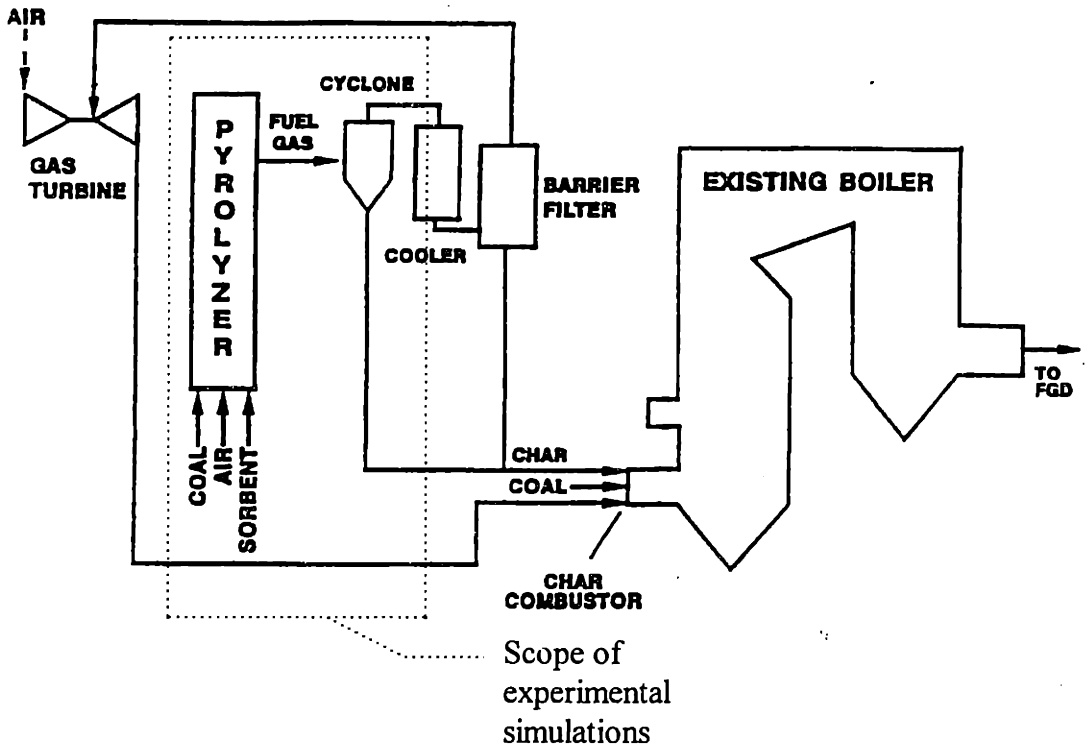

Figure 1-3 Scope of Experimental Simulations Pertaining to this Thesis Work[5]

A 4/7 scaled model of the HIPPS pyrolyzer has been constructed in MIT. Solid flow behavior such as segregation and mixing of the dissimilar materials representing char and spent sorbent in the cold model should be similar to that of the pyrolyzer. Segregation and mixing can be approximately quantified by measuring local material concentration along different locations of the riser through the use of sample ports. (Section 2.5) The trend of segregation and mixing under different operating conditions are of special interest. The particle size distribution of samples collected at the ports are also analyzed for a better understanding of mixing and segregation relative to particle sizes. Lastly, the solid concentration along the riser should exhibit similarity between the pyrolyzer and the cold model as well. Solid concentration are measured by the differential pressure drop along different locations in the riser. Volumetric solid fractions (dimensionless) are

calculated based on the differential pressure measurements and thus provide a basis for comparison between the hot bed and cold model. In short, by studying the material concentrations along the riser at different locations; their respective particle size distributions; and the volumetric solid fractions along the riser, the hydrodynamic behavior of a fluidized bed of dissimilar materials can begin to be understood and quantified.

At the present time, exact compositions of limestone and char in the pyrolyzer at steady state are unknown as hot bed tests have not been carried out. Although predictions have been made on the coal and limestone feed rate and the char and spent sorbent conversion rate, the individual solid entrainment rate at steady state at a given superficial gas velocity is unknown. As a result, the cold model test in its initial stage includes several dissimilar char/sorbent mixtures to approximately cover the range of actual conditions and to simulate the steady state material concentration of the hot bed.

[5] Extracted from FWDC on HIPPS final report.

2. Experimental Setup and Operating Conditions

This chapter describes in detail the experimental equipment used in the MIT lab scale cold model, selected solid bed materials and their properties, application of simplified scaling laws to the cold model, sampling apparatus and analysis procedure, and instrumentation. The level of detail especially in the cold model description is intended for readers who are potentially interested in reproducing the experiment. The operating conditions in both the pilot plant and the cold model will also be described in detail.

2.1 Foster Wheeler Pilot Plant Physical Description

The pyrolyzer is circular with a 7-inch ID through out its height. The distance from the center of the recirculation inlet to the center of the outlet near the top is 32'-3 3/8". The exit section has an abrupt 90° geometry that allows solid material to exit through a 3" ID section into the primary cyclone. Refractory material is used for the inside lining of the pyrolyzer wall.

The distributor consists of a 1" core for injection of solid materials (coal and sorbent) while a 1 ½" annular region supplies additional air needed for the fluidization process. Recirculation of solid materials that return from the primary cyclone is made possible by the utilization of a nitrogen aerated non-mechanical J-valve. In this particular pyrolyzer, secondary air supply is absent; fluidization gas is supplied entirely through the distributor at the bottom of the bed.

Since elaborative detail description of the Foster Wheeler Pilot Plant Pyrolyzer can be redundant for the scope and objective of this thesis, only the dimensions relevant to the hydrodynamic scaling will be stated and they can be found in Figure 2-1 .

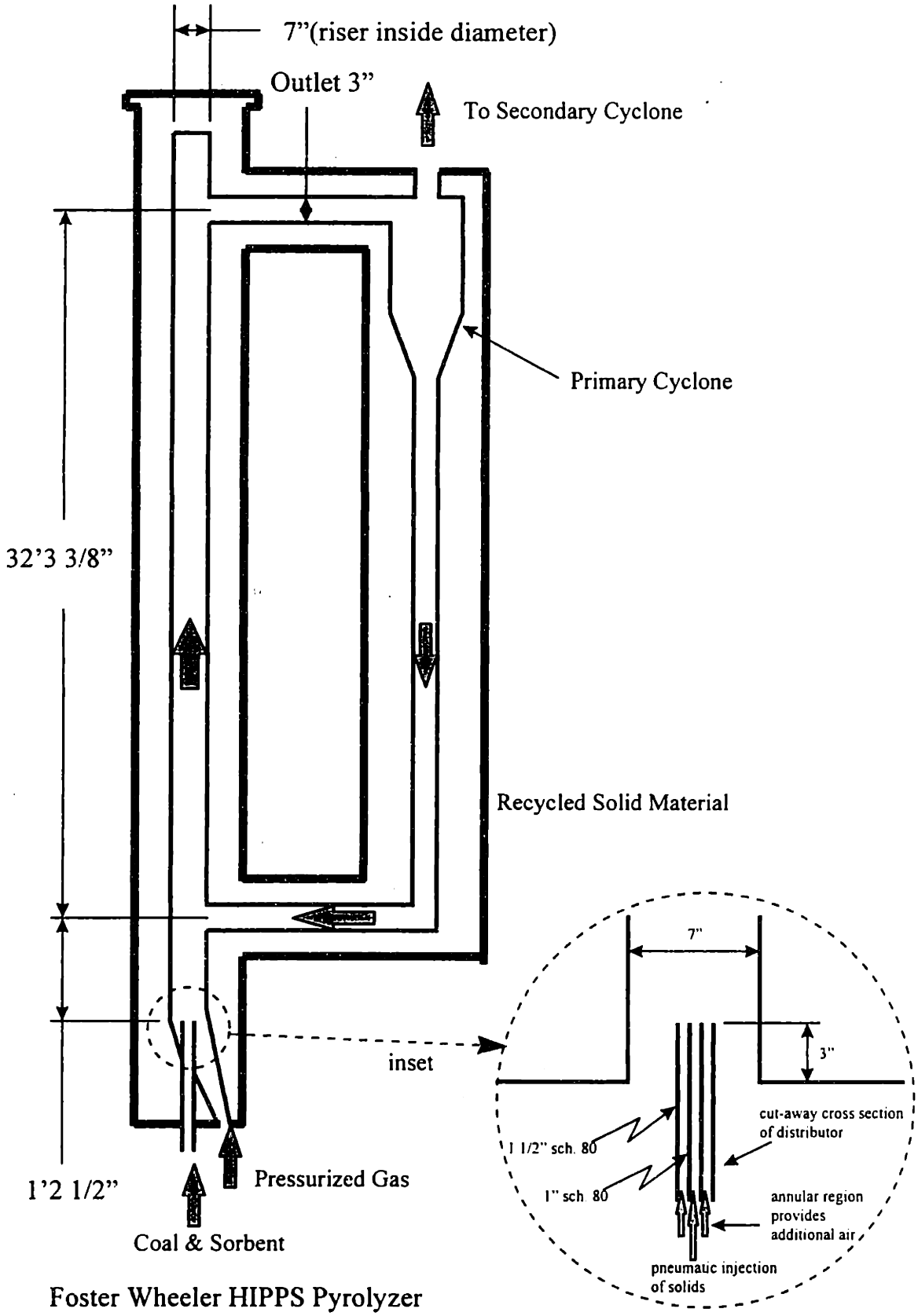

Figure 2-1 Dimensions of Foster Wheeler Pilot Plant Pyrolyzer

2.1.1 Pilot Plant Operating Conditions

The important operating parameters in the pilot plant which are pertinent to the application of the scaling law include riser velocity or superficial gas velocity, pressure, and temperature. The rate at which coal and sorbent are introduced into the system is also important in the understanding of the steady-state composition of char and spent-sorbent in the riser.

A number of test runs will be made by Foster Wheeler Development Corp. The following table (Table 2-1) summarizes the operating conditions at which tests will be performed.

Test #	Riser Vel. (ft/s)	Pressure (psia)	Temp. (°F)	Fuel Gas (lb/hr)	Char Rate (lb/hr)	Lime Rate (lb/hr)
1	5	206	1700	1098	85	29
2	6	206	1700	1318	102	35
3	7	206	1700	1537	134	43
4	8	206	1700	1757	153	50
5	9	206	1700	1977	195	60
6	10	185	1700	1977	195	60
7	11	168	1700	1977	195	60
8	12	154	1700	1977	195	60

Table 2-1 Foster Wheeler Development Corp. Pilot Plant Test Matrix

2.2 Hydrodynamic Scaling Calculations

Using the simplified set of hydrodynamic scaling relationships for pressurized fluidized bed combustors developed by Glicksman (1988), a lab scaled cold model can be constructed. The particles in the lab scale cold model is expected to exhibit a similar hydrodynamic behavior as that of the hot bed or pilot plant if the scaling laws are obeyed faithfully, as verified by Glicksman *et al* (1995). Particles in the cold model are fluidized with air at ambient pressure and temperature. This section will focus on how the pilot plant dimensions and operating conditions are translated into the lab scale cold model through the use of the simplified set of scaling laws. The cold model material properties such as particle density and mean particle diameter of the cold model are of particular interest. They can be easily characterized by utilizing the scaling laws.

The simplified set of scaling laws is as followed:

$$\frac{\rho_s}{\rho_f} \quad \frac{u_o^2}{gD} \quad \frac{u_o}{u_{mf}} \quad \frac{L}{D} \quad \frac{G_s}{\rho_s u_o} \quad \phi_s \quad PSD$$

where ρ_s and ρ_f are the densities of solid particles and gas respectively. Definitions of the remaining symbols can be found in chapter 1.2. Upon selection of a scale factor for the linear dimensions with the known operating characteristics of the hot pilot plant, the following steps can be carried out to determine cold model (I) particle material density, and (II) mean particle diameter. For convenience and consistency, calculations and their results are presented in SI units.

- Select a riser diameter for the cold model, D_{cold} from a given D_{hot}
- Determine $\left.\frac{\rho_s}{\rho_f}\right|_{hot}$ for pilot plant; equate with $\left.\frac{\rho_s}{\rho_f}\right|_{cold}$; find $\rho_s\,|_{cold}$
- Match $\left.\frac{u_o^2}{gD}\right|_{hot} = \left.\frac{u_o^2}{gD}\right|_{cold}$ and determine $u_o|_{cold}$

- Obtain $\overline{d_p}\big|_{hot}$ and determine $u_{mf}\big|_{hot}$, thus $\frac{u_o}{u_{mf}}\Big|_{hot}$

  The relationship used for u_{mf} calculation is Ergun equation with modifications by Wen and Yu (1966). i.e. for $\mathrm{Re}_p = \frac{\rho_g u_o d_p}{\mu} < 20$

$$u_{mf} = \frac{\overline{d}_p^2(\rho_s - \rho_g)g}{1650\mu}$$

  where μ is the fluid viscosity.

- Equate $\frac{u_o}{u_{mf}}\Big|_{hot} = \frac{u_o}{u_{mf}}\Big|_{cold}$ and find $u_{mf}\big|_{cold}$

- Find $\overline{d_p}\big|_{cold}$ from $u_{mf}\big|_{cold}$ since $u_{mf}\big|_{cold}$ is a function of $\overline{d_p}\big|_{cold}$

The table below summarizes the results of calculations for both char and sorbent.

	Char		Sorbent	
	hot	cold	hot	cold
Scale Factor[6]	1.75	1	1.75	1
ρ_s [kg/m^3]	577	***232***	1922	***902***
ρ_f [kg/m^3]	2.94	1.18	2.94	1.18
$\bar{u}_o$ [m/s]	2.74	***2.07***	2.74	***2.07***
$\overline{d_p}\big\|_{hot,given}$ [microns]	46		189	
$u_{mf}\big\|_{hot}$ [m/s]	0.000152		0.010027	
$\frac{u_o}{u_{mf}}$	18070		273	
$u_{mf}\big\|_{cold}$ [m/s]		.000115		.00758
$\overline{d_p}\big\|_{cold,calculated}$ [microns]		39		162

Table 2-2 Summary of Calculated Properties of Cold Model Particles using Simplified Scaling Laws

[6] The scale factor is determined from linear dimensions; hot bed height L_{hot} = 32'-3 3/8" and hot bed diameter D_{hot} = 7", and L_{cold} = 18.8' and D_{cold} = 4".

2.3 MIT Lab Scale Cold Model Physical Description

The lab scale cold model is 1/7 the size of the Foster Wheeler pilot plant. The distance between the inlet and the outlet is 18.8 ft while the inside diameter of the riser is 4 inches. Thus, conforming to the $\frac{L}{D}$ ratio of 56, identical to that of the pilot plant. The riser section is constructed exactly to scale while the return leg and the cyclones are not matched proportionally. The latter are believed not to affect the hydrodynamic behavior of interest. (Hyre, 1995)

The main riser section is constructed with a series of sch. 40 4-inch transparent PVC pipes joined together by PVC flanges. The distance between the inlet and outlet was described above while the distance from the outlet to the top of the riser is an additional 1 ½ ft such that an abrupt exit section is formed. Both the exit and the entrance sections are attached to the riser section by 4" Sch. 80 PVC tee's. The exit section has a 1 ½-inch I.D. pipe that is scaled to exactly half of that of the pilot plant. Pressure taps (6 in total) have been drilled axially along the wall of the riser at 45° downward so as to prevent as much as possible the accumulation of particles at the tap openings, assuming the annular-core model applies.

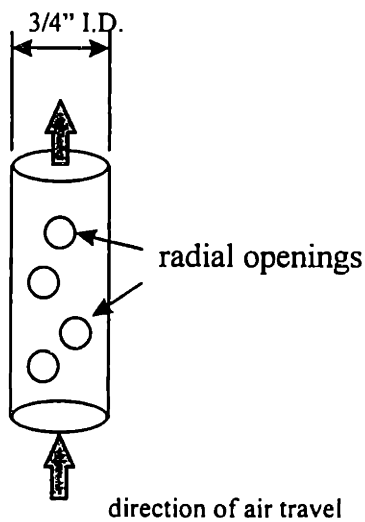

Figure 2-2 Geometry and Design of the Distributor

The distributor is built to scale and is directly located at the very bottom of the riser. It is constructed from a ¾" Sch. 80 PVC pipe and is about a foot in total length. Numerous holes or small openings with approximate diameters of ¾" are drilled along the radial length of the distributor pipe so as to allow a more uniform fluidization effect. A drawing of the distributor is shown in Figure 2-2 .

The primary cyclone acts as the separation device. It is constructed from ¼" Plexiglas which forms the main section of the cyclone with an inside diameter of 9 7/16". The main section is 18" in height. The bottom section is also 18" in height but is tapered from a diameter of 9 7/16" to 2"; solid particles moving tangential to the inside surface of this taper section gradually acquire higher angular velocity and readily settle to the primary return leg for recirculation. Air and finer particles which escape the primary cyclone separation exit through a 4" I.D. section located near the top of the cyclone and into the entrance of a secondary cyclone. The return leg of the secondary cyclone is connected back to the primary return leg through a series of 2" Sch 80 PVC transparent pipe. A 1" PVC ball valve is installed in the return of the secondary cyclone and shut to prevent backflow of particles and air during the operation of the riser. The ball valve is open and particles accumulated in the secondary return leg during the run are returned to the primary return leg. A filter box is connected to the exhaust of the secondary cyclone to filter out any extra fines which escape both the cyclone separations. The filter box contains a high density microfine glass fiber prefilter and a hepa filter.

The primary return leg has markings on its transparent wall so that the time particles take to move through the known distance as denoted by the markings can be measured. This process allows one to measure the solid recirculation rate. Plug flow within the return leg is a necessary condition for this method of flux measurement to hold.

A non-mechanical L-valve is used to control the amount of particles from the return leg to be recirculated. The L-valve consists of a series of taps with controllable air pressure from the shop air supply. Compressed air enters the taps through a series of needle valves

and into the return leg. Particles accumulated in the primary return leg are aerated by the shop air and 'escape' into the riser section. By varying the amount of air injected into the return leg, the amount of particles being recirculated can also be varied. This method works best when the particles in the primary return leg are not fluidized from the effect of L-valve. If there is sufficient particles in the primary return leg, this problem can be avoided.

An orifice plate of 2.094" I.D is used indirectly for the measurement of superficial gas velocity. This obstruction metering method (Beckwith, Marangoni & Lienhard 1993) introduces a pressure drop across the orifice plate upstream of the distributor. With known temperature of compressed air and back pressure, volumetric flow rate of air and velocity of air at any given cross section area can be calculated. Detail of measurement will be given in section 2.6.1.

Five sample ports capable of drawing solid samples from the riser during a test run are installed throughout the model. Four of the five sample ports are installed and spaced evenly along the entire height of the riser. The last of the five port is placed just before the entrance of the primary cyclone and after the exit from the riser to capture a representation of particles escaping the riser. More details about sample ports will be given in section 2.5.

2.3.1 Lab Scale Cold Model Operating Conditions

The material used to represent char in the lab scale cold model is granulated wood cork while polyethylene plastic represents spent sorbent. Their properties will be discussed in detail in the next section. The actual composition of both char and spent sorbent within the pyrolyzer depends on the operating conditions which can vary from case to case. The cold model, however, is less flexible in altering the relative composition of the mixture within each run since particles recirculate in a close loop system. Therefore, different

mixture compositions are used in the cold model at the same test conditions. For instance, under the same superficial gas velocity, 25% and 50% by mass of polyethylene plastic will be used.

The corresponding cold model superficial gas velocity can be calculated using the Froude number from the scaling law; $Fr = \frac{u_o^2}{gD}$, where $u_o|_{cold} = u_o|_{hot} \bullet \sqrt{\frac{D_{cold}}{D_{hot}}}$

2.4 Bed Materials/Particles

This section documents in detail the both the material in the hot bed and that selected for the cold model.

2.4.1 Properties of Bed Materials - Foster Wheeler Pilot Plant

The most critical properties relevant to the scaling law are Particle Size Distribution (PSD), sphericity and Material Density. The solid-to-gas density ratio ($\frac{\rho_s}{\rho_f}$), sphericity and the dimensionless PSD must be matched closely as defined by the scaling law.

Coal and Limestone are fed into the pyrolyzer as raw feed stock together with air. Chemical reactions take place within the pyrolyzer and form both gaseous and solid products. The solid products being char and spent sorbent. Under steady state conditions, there should be a fixed composition of each of the solid products remaining in the pyrolyzer. The material properties of solid products of both char and spent sorbent are of special interest.

Solid Product - Spent Sorbent

The dimensional PSD as predicted and supplied by Foster Wheeler is plotted in the following plot. The sauter mean particle size is 189 microns. And the maximum particle size range is about nine times the mean.

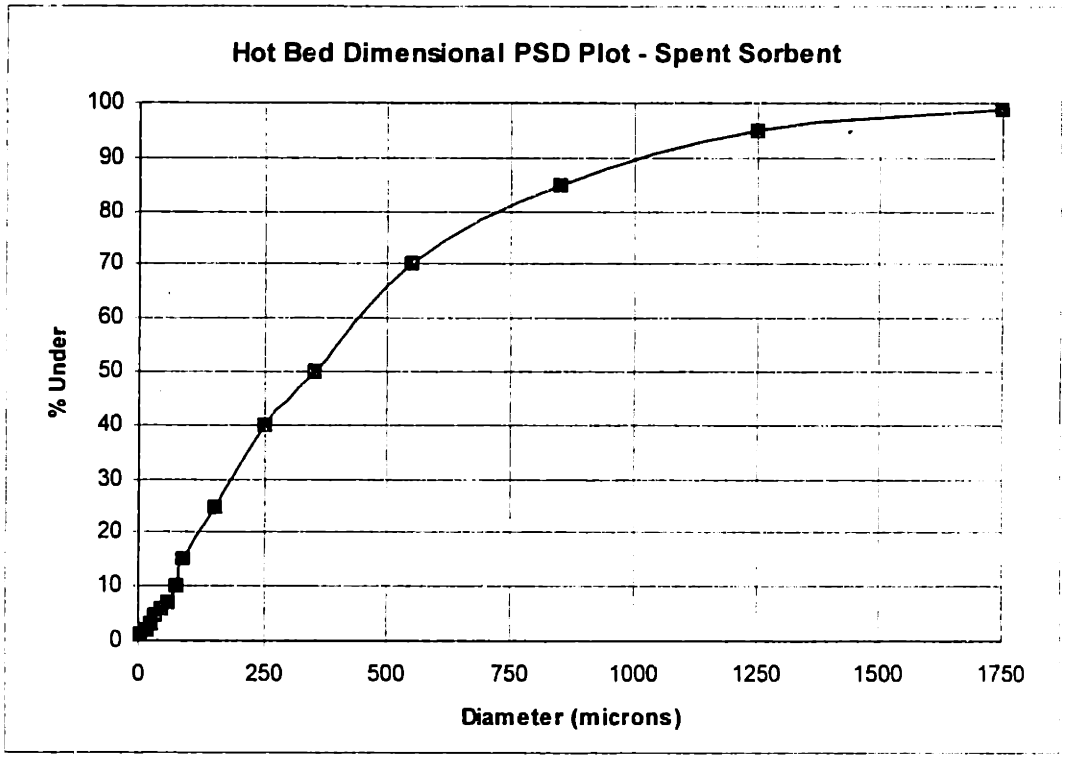

Figure 2-3 Foster Wheeler Hot Bed PSD - Spent Sorbent

Spent sorbent consists of approximately fifty percent of calcium carbonate and fifty percent of calcium sulfide under a reducing environment as that of the pyrolyzer. Spent sorbent and char samples extracted from the primary cyclone of the Foster Wheeler pilot plant have been analyzed. Char can be separated from spent sorbent using 'floater-sinker' method[7] and the latter was analyzed for density. Experimental measurement of spent sorbent density is approximately 2.1 g/cm^3. Standard chemistry handbook (Weast, 1977) estimation of spent sorbent of above approximated composition yields a density of 2.4 g/cm^3. Thus density of spent sorbent is estimated to be 2.24 g/cm^3 (2243 kg/m^3) or 140 lb/ft^3. (Appendix A)

[7] Water at room temperature was used as the medium to separate char of density approximately .58 g/cm^3 from spent sorbent of density about twice of that of water.

Solid Product - Char

The dimensional plot of PSD of char is plotted in Figure 2-4 . The sauter mean of char is 46 microns and the material density is 36 lb/ft^3 or 577 kg/m^3 as supplied by Foster Wheeler.

The sphericity of a particle can be measured by taking the ratio of the surface area of a perfect sphere over the surface area of the particle. Since there is no easy technique for the separation of char and spent sorbent, the mixture supplied by Foster Wheeler was used for the measurement of sphericity instead of using each specie. It has been found that the average sphericity of the mixture is about 0.65.

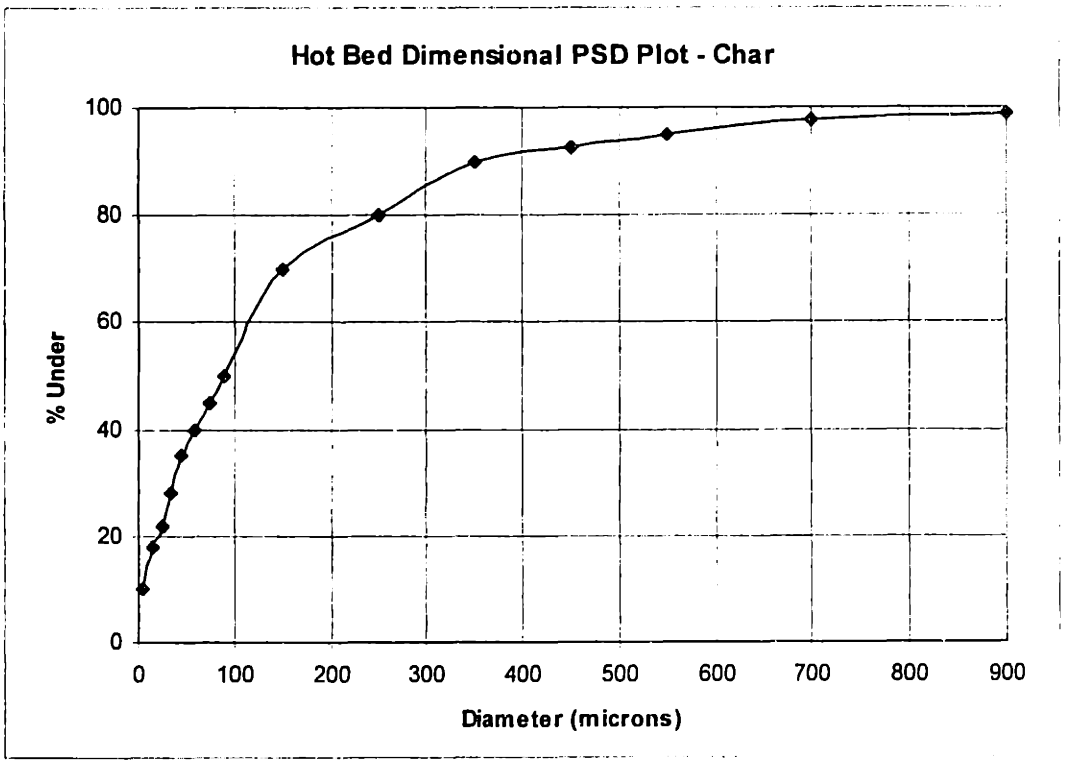

Figure 2-4 Foster Wheeler Hot Bed PSD - Char

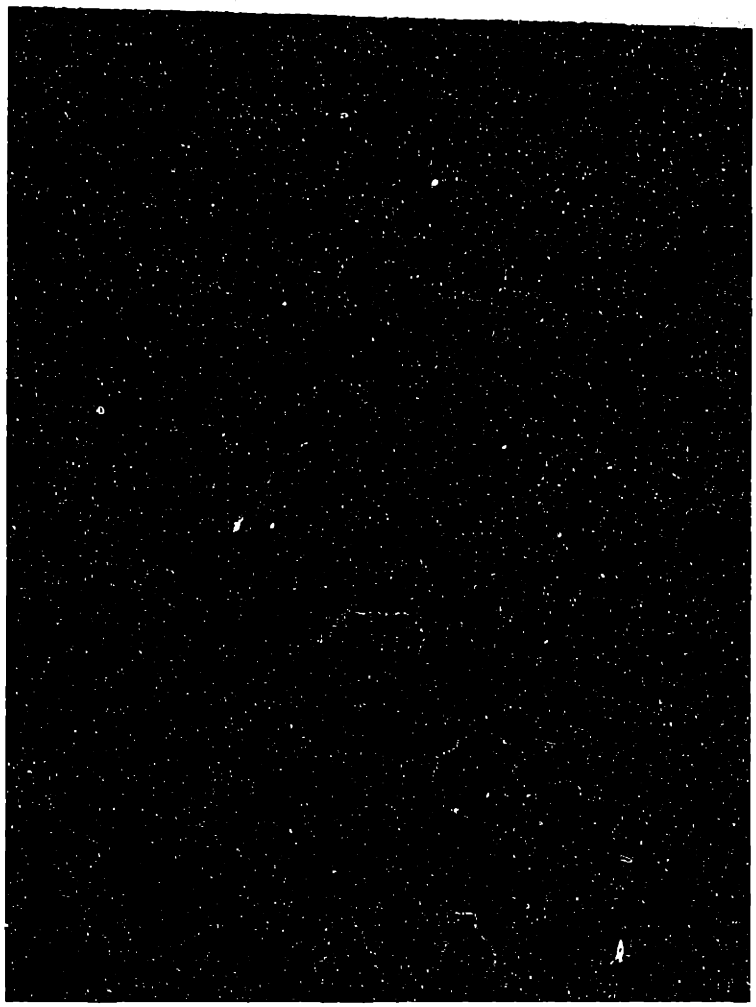

Figure 2-5 Microscopic View of Char and Spent Sorbent Particles [x 50]

2.4.2 Selection of Cold Model Particles

The properties such as material density and the mean particle diameter for the cold model have been calculated in Table 2-2 . The material density representing char in the cold model should be around 232 kg/m^3 while that of spent sorbent is about 902 kg/m^3. The

mean particle size simulating char should be 39 microns while that of spent sorbent is 162 microns.

Different particles of relevant densities, particle size distribution and sphericity have been identified. Material density can be measured by a helium pycnometer while the particle size distribution can be measured by simply using mechanical sieves with different sizes. In some instances, particle size distribution is supplied by the vendor. Sphericity measurement technique was mentioned in the previous section.

Char

Materials have been identified that could potentially be suitable for the equivalence of cold char particles. They include wood flour, granulated cork wood and hollow glass spheres. Their respective properties and suppliers have been listed in detail in Appendix B. Criteria for selection include material density, sphericity and particle size distribution. The effect of static electricity of the material was also taken into consideration in the selection process. The selected material for our application is granulated cork wood; its properties will be described in the next section.

Spent Sorbent

Polyethylene plastic stands out to be the best matching material as identified by Hyre (1995) as it has the appropriate material density and particle size range. The particle size distribution spans across a wide enough spectrum for the duplication of the hot particle size distribution. Its properties will be described in the next section.

2.4.3 Properties of Bed Materials - MIT Scaled Cold Model

Char

The material chosen to simulate char in the cold model is granulated cork wood from Maryland Cork Company, Inc. The cork has a measured average bulk density of 203 kg/m^3 and an average solid density of 242 kg/m^3 with an assumed average void fraction of 16.25%.

The cork comes in two distinct size ranges. One of them is mesh 80/0 (smaller than 177 microns) and the other is mesh 40/80 (between 177 microns and 420 microns). The former is termed fine cork while the latter is termed coarse cork. Coarse cork has a measured bulk density of 250 kg/m^3 and an assumed particle void fraction of 20%. This yields a solid density of 313 kg/m^3 for the coarse cork. The measured bulk density of fine cork is 185 kg/m^3 with an assumed particle void fraction of 15%. Thus the solid density of fine cork is 218 kg/m^3. By mixing one part of coarse cork to three parts of fine cork, the average solid density for the cork mixture is thus 242 kg/m^3 and a bulk density of 203 kg/m^3 as quoted in the beginning of this section. This method of calculating solid density is based on the assumption that addition of particles of two different sizes do not alter their individual particle void fraction. This method serves as an approximation.

It has been found that mixing approximately 75% by mass of the mesh 80/0 (fine) cork with 25% by mass of the mesh 40/80 (coarse) cork also gives an approximately similar particle size distribution as required. Particles have been sieved to obtain necessary particle size distribution. The results of PSD analysis for both fine and coarse cork is tabulated in Table 2-3

Granulated Cork wood							
Range			range average	mass of cork	mass frac.	dimensionless dia.	cum. freq(%)
(micron)			(micron)	(g)		(by dp mean)	cold-cork
0	-	38	19	3	0.015	0.475	1.485
38	-	45	41.5	9	0.045	1.038	5.941
45	-	53	49	10	0.050	1.225	10.891
53	-	63	58	20	0.099	1.450	20.792
63	-	75	69	19	0.094	1.725	30.198
75	-	90	82.5	18	0.089	2.063	39.109
90	-	106	98	17	0.084	2.450	47.525
106	-	125	115.5	21	0.104	2.888	57.921
125	-	149	137	21	0.104	3.425	68.317
149	-	180	164.5	12	0.059	4.113	74.257
180	-	212	196	15	0.074	4.900	81.683
212	-	297	254.5	14	0.069	6.363	88.614
297	-	355	326	9	0.045	8.150	93.069
355	-	500	427.5	14	0.069	10.688	100.000
			sum	202			

Table 2-3 PSD Analysis of Fine and Coarse Cork

The mean particle diameter, $\overline{d_p}$ has been calculated to be 92 μm. $\overline{d_p}$ has been calculated using

$$\overline{d_p} = \frac{1}{\Sigma'(\frac{x}{d_p})_i}$$

where x is the mass fraction and d_p is the average diameter of a given range. d_p is derived from the sum of limits divided by two in any given range.

A dimensionless particle size distribution plot with both the cork (cold) and the char (hot) is presented below. It has been non-dimensionalized by the average desired mean particle diameter of 40μm. Typical cork particles are shown in Figure 2-7 .

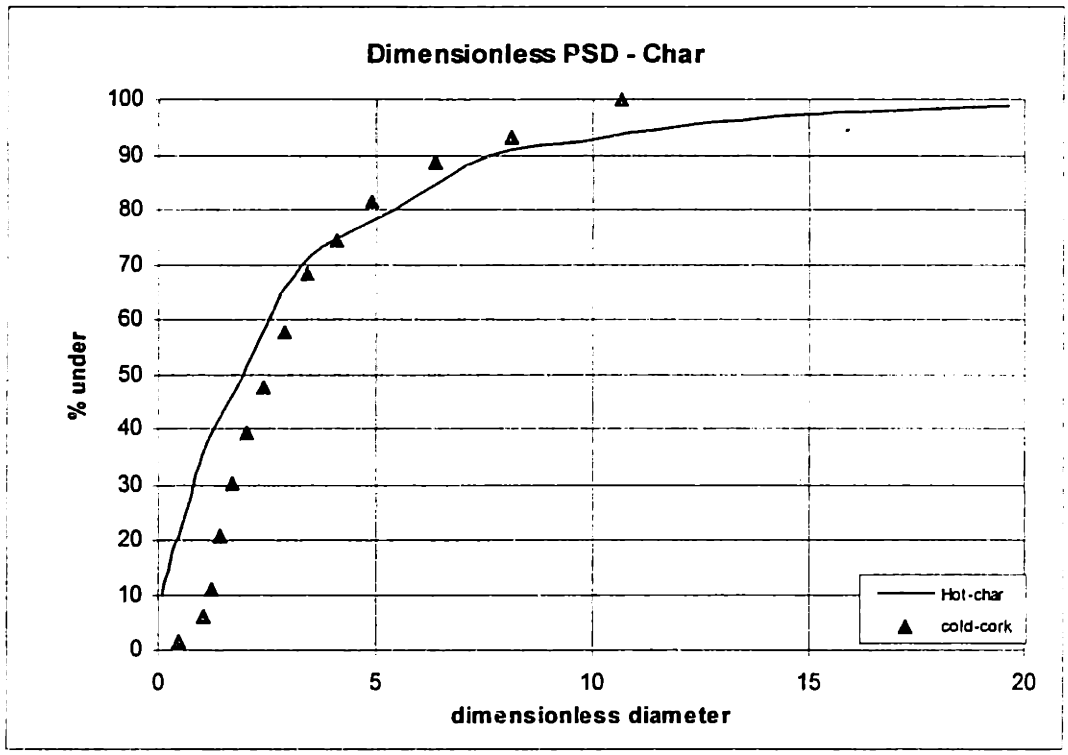

Figure 2-6 Dimensionless PSD plot of char (hot) and cork (cold)

Average sphericity of cork of both coarse and fine was measured to be 0.76 using optical microscope. The image obtained from the microscope was scanned and analyzed by a computer imaging software to obtain surface area and perimeter of each individual particle. Sphericity can be calculated by the following equation:

$$\Phi = \frac{4 \cdot \pi \cdot A}{p^2}$$

where p and A are perimeter and surface area of a particle. A summary of the properties of cork and char are presented in Table 2-5

Figure 2-7 Microscopic View of Granulated Cork Wood Particles (Coarse) [magnification ~ x 100]

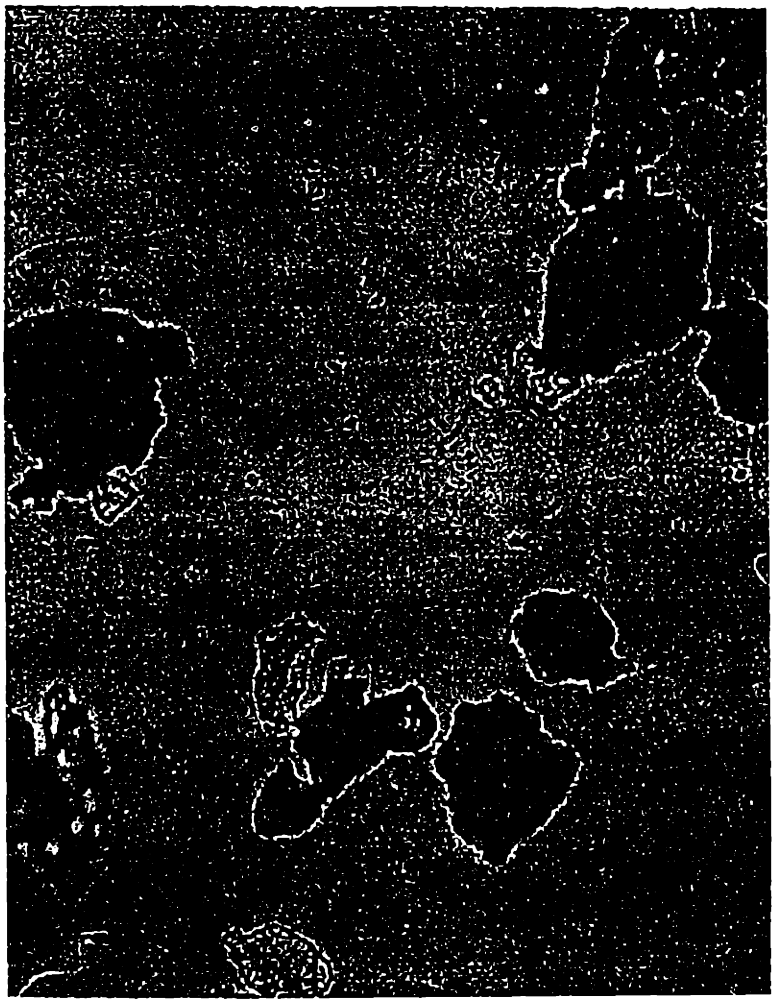

Figure 2-8 Microscopic View of Granulated Cork Wood Particles (Fine) [magnification ~ x 200]

Spent Sorbent

The material selected to simulate spent sorbent in the cold model is polyethylene plastic with a material density of 902 kg/m^3 as measured by a helium pycnometer. In addition of being a material of the appropriate density, polyethylene particles also comes in a wide variety of sizes. This allows particles to be sieved to give a closely matched PSD. Plastic particles have been sieved to custom match the PSD of the hot bed and results are tabulated in Table 2-4

PSD of plastic - cold model							
			range ave.	mass obtained	mass frac	dimensionless dp	cum freq(%)
Sieve Size Range (micron)			(micron)	(g)			cold-plastic
0	-	38	19	0	0.000	0.119	0.000
38	-	63	50.5	0	0.000	0.316	0.000
63	-	75	69	12	0.006	0.431	0.628
75	-	125	100	122	0.064	0.625	7.012
125	-	180	152.5	117	0.061	0.953	13.134
180	-	212	196	260	0.136	1.225	20.740
212	-	297	254.5	340	0.178	1.591	44.532
297	-	355	326	180	0.094	2.038	53.951
355	-	500	427.5	200	0.105	2.672	64.417
500	-	710	605	320	0.167	3.781	81.162
710	-	1000	855	200	0.105	5.344	91.627
1000	-	1400	1200	160	0.084	7.500	100.000
			sum	1911			

Table 2-4 PSD Analysis of Plastic Particles

The mean particle diameter is calculated as 283 μm using the same formula as that of cork. The desired mean particle diameter is approximately 160 μm.

The figure below presents the dimensionless comparison of particle size distribution between the hot and cold bed and it is non-dimensionalized by the desired mean particle diameter of 160 μm. Figure 2-10 is a microscope photograph of some typical plastic particles.

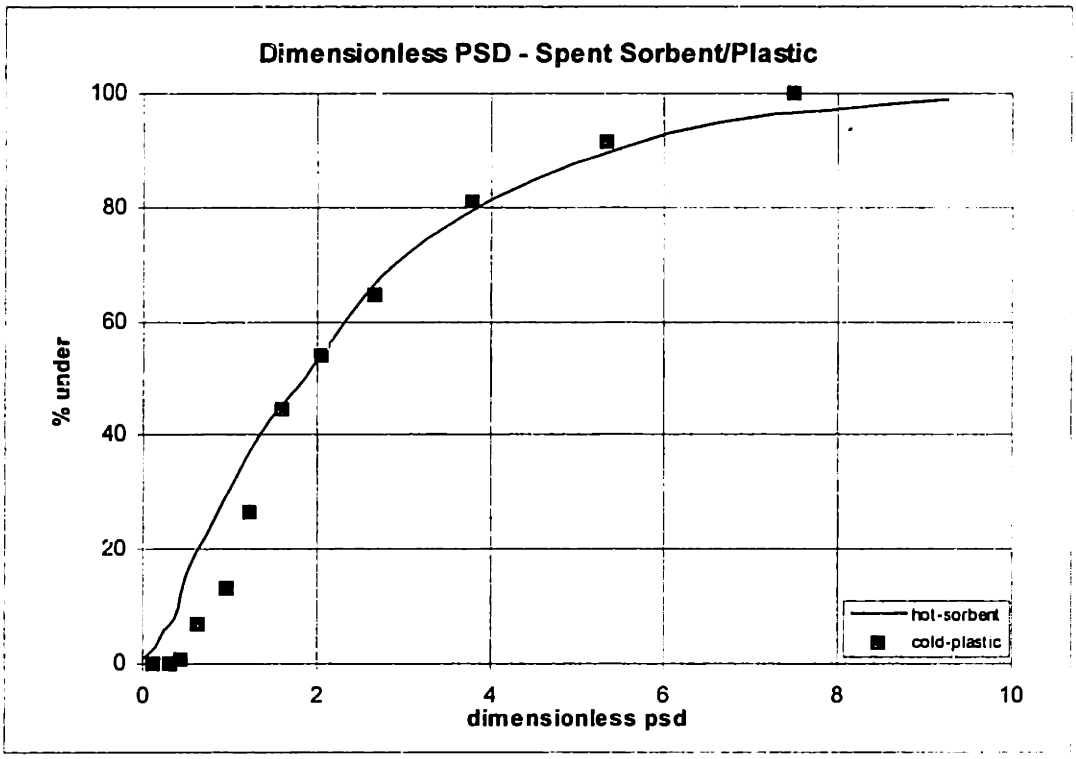

Figure 2-9 Dimensionless Plot of Spent Sorbent (hot) and Plastic (cold)

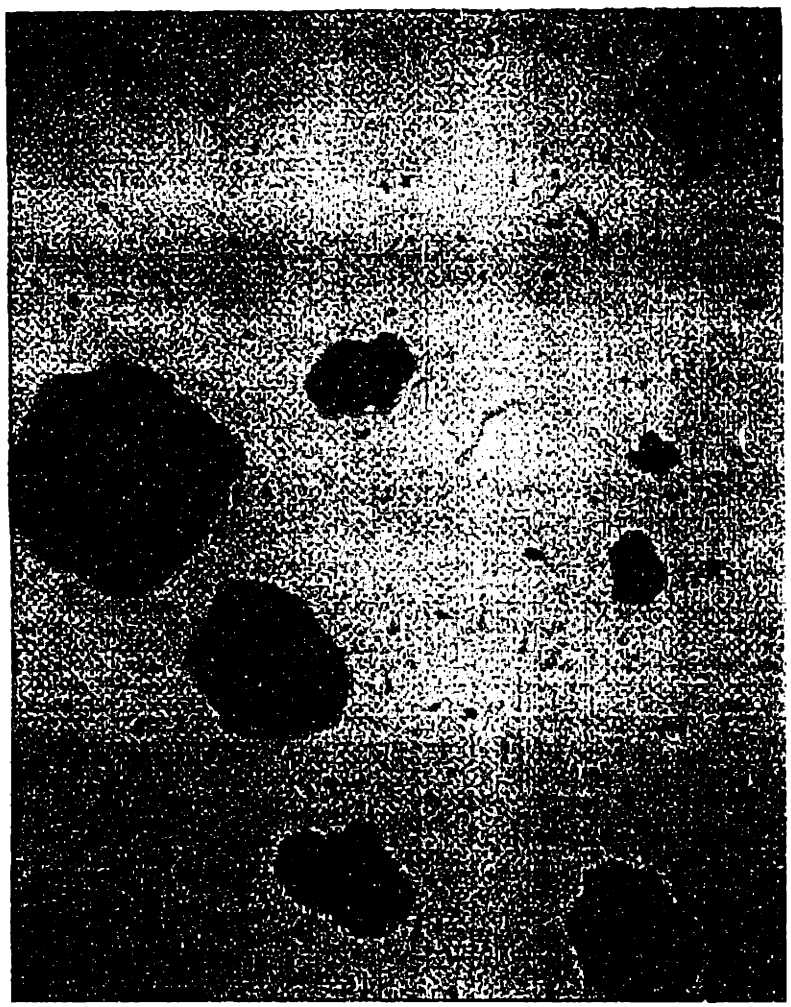

Figure 2-10 Microscopic View of Polyethylene Plastic Particles

[magnification ~*x* 50]

The table below presents a summary of comparison of material properties between the cold and the hot bed.

	Char		Spent Sorbent	
	Hot	Cold	Hot	Cold
Material	char	granulated cork	spent sorbent	polyethylene plastic
Operating Temp (K)	1200	300	1200	300
Operating Pres. (KPa)	1013.3	101.3	1013.3	101.3
Solid Density, ρ_s (Kg/m^3)	577	242	2240	905
Gas Density, ρ_g (Kg/m^3)	2.94	1.184	2.94	1.184
ρ_s / ρ_g	**196**	**204**	**762**	**764**
PSD	matched		matched	
Sphericity	0.646 [8]	0.76 [9]	0.646	0.78
Mean Particle Diameter (μm)	46	40	190	160
Superficial Gas Vel, U_o (m/s)	2.74	2.07	2.74	2.07
Min. Fluidization Vel U_{mf}(m/s)	1.52e-4	1.15e-4	1.00e-2	.758e-2
U_o / U_{mf}	18026	18000	274	273

Table 2-5 Hot and Cold Material Properties Comparison Summary

[8] Sphercity measured from a mixture of char and spent sorbent sample supplied by Foster Wheeler. Thus, this is an average value for the two types of materials.

[9] Values obtained from the Massachusetts Institute of Technology UROP report by Anand Devendran, titled "Determining the sphercity of particles for fluidized beds".

2.5 Sample Ports - MIT Cold Model

When dissimilar solids are fluidized, the understanding of local solid concentration along the riser can give an insight to the mixing and segregation mechanism of the system. Through the use of several sampling devices at discrete locations along the riser, samples of mixture can be collected and analyzed for both concentration and particle size distribution.

2.5.1 Physical Description - Design and Location - Cold Model

Major components of the cold model sample port includes a ⅜" I.D. probe, an actuated ball valve, cyclone, particle collection port, filter compartment, and a rotameter.

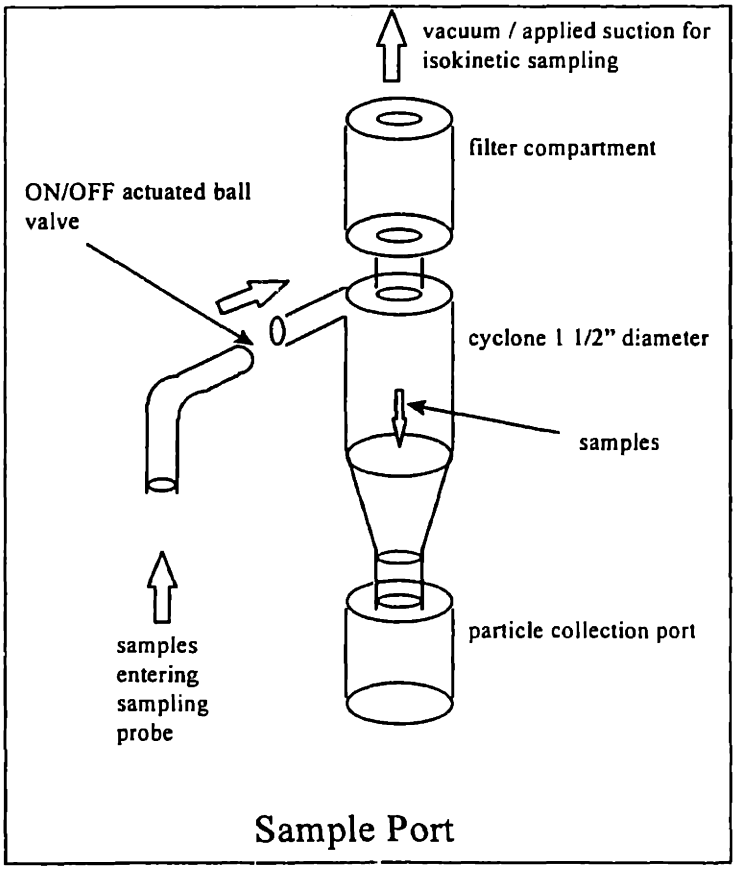

Figure 2-11 A Wire Frame Model of a Sample Port

The ⅜" I.D. probe is made of copper. It is bent at a 90° angle with a radius of approximately 1". The entrance of the probe is facing directly downward in the center of the riser so as to capture particles in the lean phase or core region of the core-annular model. Particles entering the probe will gradually decelerate by traveling around the radius into the entrance of the cyclone horizontally. The diameter chosen for the probe is approximately 7 -8 times the largest particle diameter in the bed to ensure inclusion of largest particles in the sampling process.

An actuated ball valve (Model #: Omega FVL5800) is installed before the entrance of the cyclone. The valve controls the ON/OFF position of the sample port and it can be controlled from a switch in the control panel area. It is particularly useful for hard-to-reach sample ports located higher up in the bed. It can also help control the sampling period more precisely and consistently for all sample ports.

The cyclone consists of 1/8" thick transparent plexiglas cylinder with an I.D. of 1½ ", a conical section that tapers from 1½" to ¾" through a distance of 1 ½", and an entrance leg of I.D. of ¼". It acts as the separator of solid samples and air and helps to direct samples downward into the collection port. Air exits from the top outlet of the cyclone through a filter compartment which consists of filtration material to capture any fines that might have escaped cyclone separation. The particle collection port is a plastic container which can be removed easily from the main sample port. It is engaged by thread fitting onto the main sample port structure. It can hold upto 150 cm^3 of samples.

It is not our interest to perform precise isokinetic sampling, as was done by Herb *et al* (1992). Sampling approximately at isokinetic condition and having the aspiration velocity matching the superficial gas velocity would be acceptable for our application. A schematic of solid sampling apparatus is shown in Figure 2-13 . Eductors (Figure 2-12) are used to create low pressure in a vessel which eventually becomes a vacuum chamber. A supply line is connected to each sample port from the vacuum chamber through a

rotameter and a needle valve which controls the amount of vacuum each port receives. Average inlet area of the probe is measured and the desired velocity in the probe is set equal to the superficial gas velocity in the riser during sampling. Volumetric flow rate in and out of the sample port can thus be calculated. For example, if the area of the probe, A_{probe} is 2.92e-5 m^2, and the desired sampling superficial gas velocity, U_o and thus the aspiration velocity is 2 m/s, then volumetric air flow rate through the probe, Q_{probe} can be calculated by (as shown in Table 2-6)

$$Q_{probe} = U_o \bullet A_{probe} \text{ or } = 2 \times 2.92e\text{-}5 = 5.84e\text{-}5 \ m^3$$

Using the rotameter to monitor the gas flow rate of each sample port, quasi-isokinetic conditions can be obtained.

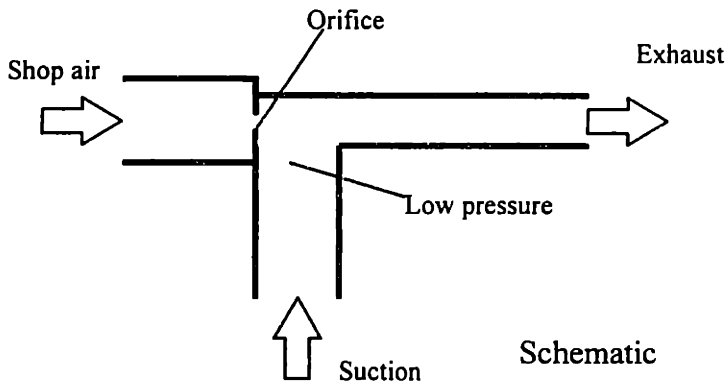

Figure 2-12 An Eductor - used for suction sampling

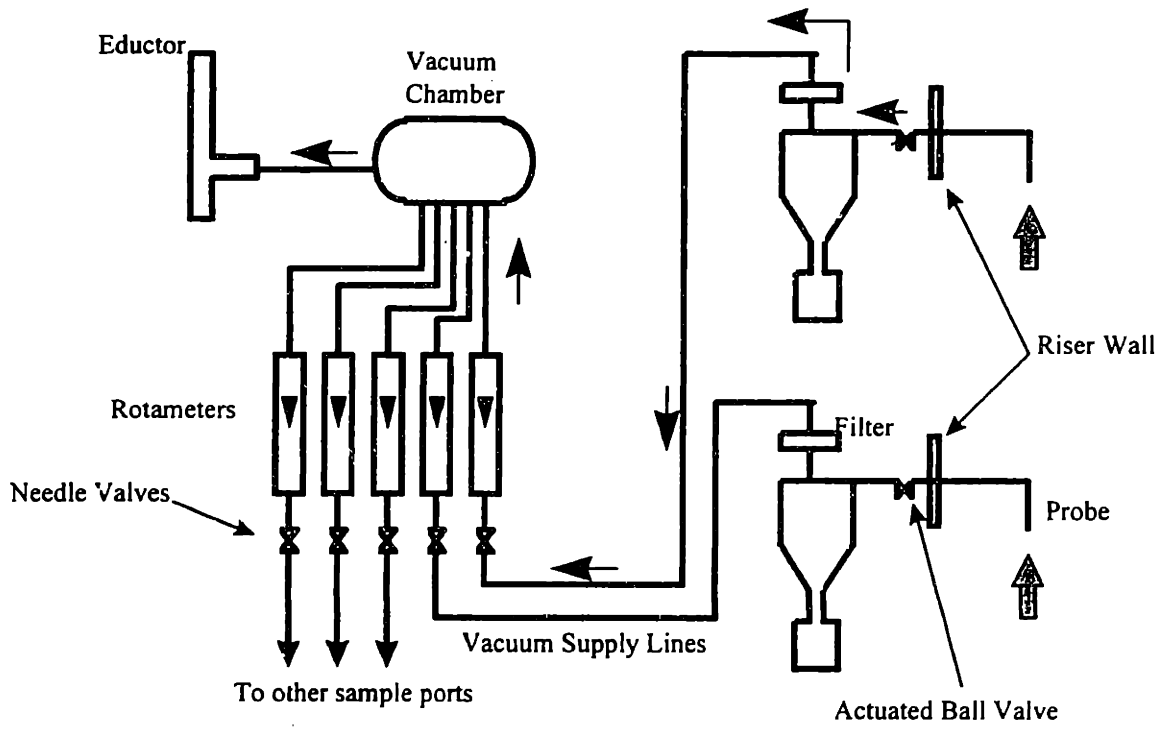

Sampling Apparatus Schematic

Figure 2-13 Sampling Apparatus Schematic

Due to economics and simplicity in construction of a sample port, it is not completely air-tight. Under vacuum conditions air is evacuated from the sample port. There are leaks between the probe tip and the port. The leaks mostly occur at the seams of the 1 ½" cyclone. The seams are not large enough to permit particles to escape. The leakage of air due to the presence of the imperfections is approximately 15% of the supply for a given U_o as shown in Table 2-6 . To compensate for this effect, more vacuum power is supplied to each port to reach isokinetic conditions. A set of measurements has quantified the amount of vacuum needed versus the bed superficial gas velocity. The measurements were obtained using two rotameters - one at the probe and the other by the filter. (As shown in Figure 2-14) When the rotameter by the probe indicated an appropriate reading corresponding to the superficial gas velocity, the filter rotameter reading was noted and tabulated in the "Q_{filter}" column in Table 2-6

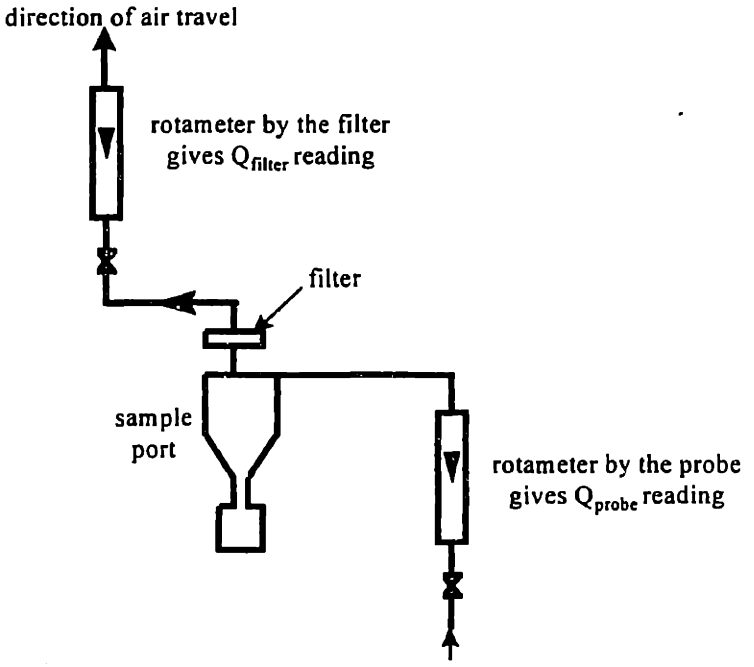

Figure 2-14 Experimental Setup for the Measurement of Vacuum by the Filter and by the Probe

Uo	Q_{probe} Vacuum	Q_{probe} Vacuum	Q_{filter} Vacuum
m/s	m^3/s	LPM	LPM
0.7	2.04E-05	1.2	1.3
0.8	2.34E-05	1.4	1.5
0.9	2.63E-05	1.6	1.7
1	2.92E-05	1.8	1.9
1.1	3.21E-05	1.9	2.2
1.2	3.51E-05	2.1	2.4
1.3	3.8E-05	2.3	2.6
1.4	4.09E-05	2.5	2.8
1.5	4.38E-05	2.6	3.0
1.6	4.67E-05	2.8	3.3
1.7	4.97E-05	3.0	3.5
1.8	5.26E-05	3.2	3.7
1.9	5.55E-05	3.3	3.9
2	5.84E-05	3.5	4.1
2.1	6.13E-05	3.7	4.4
2.2	6.43E-05	3.9	4.6
2.3	6.72E-05	4.0	4.8

Table 2-6 Rotameter Reading of Sample Ports with respect to Superficial Gas Velocity

There are altogether five identical sample ports through out the model; four of which are spaced evenly along the riser while the fifth one is located at the exhaust of the primary cyclone in the return leg section. By spacing numerous sample ports along the riser, the axial material concentration as a result of mixing and segregation can be understood better while the port just before the primary cyclone should capture a good representation of entrained material. Figure 2-15 shows the location of sample ports along the riser.

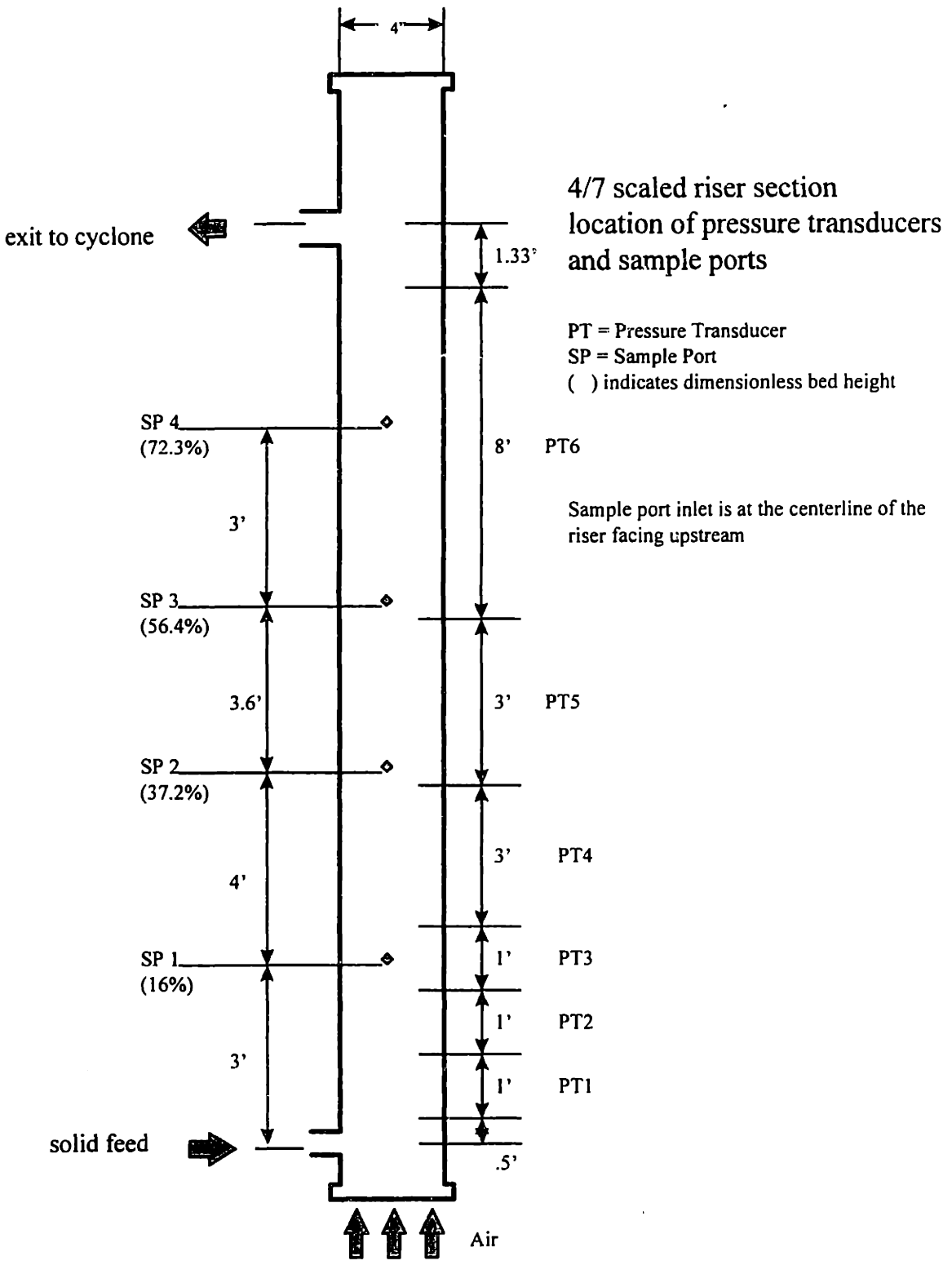

Figure 2-15 Location of Instrumentation Along Riser

2.5.2 Method of Separation of Dissimilar Solids

Dissimilar solids involved are granulated cork wood and polyethylene plastic. When samples are collected in a sample port, it is our interest to find out the amount of each of the solid material present. The mass fractions of solid materials are expected to be different along different locations of the riser due to mixing and segregation. If the cork can be completely separated from the plastic, the mass fractions x_c and x_p of cork and plastic respectively can be obtained easily. However, there has not been a simple and effective way to separate the two materials completely. A more indirect approach is taken.

By measuring the solid mixture bulk density, $\rho_{bulk|\,mix}$ in the sample port, and comparing against known bulk densities of the individual components, namely plastic $\rho_{bulk|\,p}$ and cork $\rho_{bulk|\,c}$, mass fractions x_p and x_c of both materials can be calculated and are related by the following theoretical relations.

$$x_p\,\rho_{bulk|\,p} + x_c\,\rho_{bulk|\,c} = \rho_{bulk|\,mix}$$

$$x_p + x_c = 1$$

Hirschberg *et al* (1995) used similar technique in analyzing solid concentration but he used material density rather than bulk density. Bulk density can be measured simply using a measuring cylinder and a digital scale which are readily available while solid particle densities must be measured using a helium pycnometer.

Empirical data can also be used to calibrate the measurement of the mass fractions of the dissimilar materials. By mixing known amounts of each material and measuring the resulting bulk density of the mixture, an empirical relationship between mixture composition and mixture bulk density can be established. By repeating the measurements with different material concentrations, an empirical correlation can be obtained. Results obtained from the empirical method have not deviated much from the results calculated by the theoretical linear summation assumption: $x_p\,\rho_{bulk|\,p} + x_c\,\rho_{bulk|\,c} = \rho_{bulk|\,mix}$. A comparison of the two calibration curves are shown in Figure 2-18 . The discrepancy

between the theoretical and empirical curve can be explained in terms of particle void fractions. It is observed that at a given mass fraction of plastic, the theoretical values of mixture bulk density are lower than that of the measured or empirical values. This trend can be explained by the fact that theoretical values do not reflect a change in void fractions of particles as they settle. At any given mass fraction of plastic, coarse cork particles which are small relative to the plastic particles, can fill in the voids created by the plastic particles, thus packing more particles in a given volume and increasing the bulk density in reality. Therefore, the theoretical mixture bulk density is smaller than the empirical or measured mixture bulk density at any given value of mass fraction of plastic.

Since both plastic and cork have a non-uniform particle size distribution, bulk density measurements can be made more accurate if they can be broken down into different size ranges. Each of these size ranges should have a more uniform particle size distribution and particle-particle void fraction. Thus, bulk density measurements can be made more consistently. It has been observed from the particle size distributions of both materials approximately 75% of plastic particles fall above the size of 212 μm while approximately 75% of cork particles fall under it. Thus a 212 μm sieve is used to separate the majority of the plastic from the cork in any given sample. Two calibration curves are created for particles that are larger than 212 μm; one of which is for particles mostly in the range of 212-355 μm while the other is for a range from 212 to over 1000 μm. The exact PSD of plastic particles used for these calibration curves are given in the next section (Figure 2-16 and Figure 2-17). Particles smaller than 212 μm have consistently reflected a bulk density that is identical to that of fine cork. It is thus reasonable to assume in the context of sample analysis that fine plastic particles (smaller than 212 μm) have negligible influence on the bulk density measurement.

The sample analysis procedure is as followed. The total weight of the sample collected during a test run is first weighted. The sample mixture which consists of both plastic and cork is then separated into two distinct size ranges using a 212 μm sieve with a shaker. It has been found that with the current sample collector size of 150 cm^3, a full collector

worth of sample will require approximately 5-7 min of sieving time on the shaker. The particles separated into two distinct size ranges are then weighted and recorded. Bulk density measurements are performed on the particles > 212 μm while particles smaller than 212 μm are not analyzed and are treated as cork. Particles smaller than 212 μm should contain a small fraction of smaller plastic particles as well. However, with the current bulk density measurement technique, the presence of the finer plastic particles is not detected and thus does not reflect in the bulk density reading. Finer particles are also more difficult to handle for the purpose of density measurement. For particles larger than 212 μm in a given sample, approximately half of them will be measured. For example, if there are 10 grams of particles larger than 212 μm, at least 5 grams will be measured for bulk density using a digital scale and a measuring cylinder. For volume measurement, it is crucial that the degree of compacting is consistent. All volume measurements are recorded only after rigorous tapping or compacting has been done to the sample in the cylinder until the bulk volume changes no further. The appropriate calibration curve (Figure 2-16) or (Figure 2-17) is then used to translate the bulk density of the mixture into the mass fraction of plastic for particles larger than 212 μm. Particles smaller than 212 μm contribute to the total mass of cork in the sample. Final results are presented in mass fraction of plastic of both fine (<212 μm) and coarse (>212 μm) particles.

For a 25% plastic -75% cork mixture, a typical sample collected from a sample port in the riser is about 25 g depending on the period of sampling, solid recirculation, sample port location and superficial gas velocity. About 11 g of which is smaller than 212 μm and 14 g larger than the sieve size. The 11 g are treated as cork while 7 g of the 14 g (½ of the sample) are analyzed. Typically 7 g of particles are measured in three separate times, each time measuring about 2.5 g and noting the corresponding volume. The three bulk densities are then averaged and checked against CALIBRATION CURVE I. Typical bulk density is 0.385 g/cm^3. Using the calibration curve, 54.3% is the mass fraction of plastic for particles larger than 212 μm. Including the 11 g of fine particles, the mass fraction of plastic for the whole mixture is now 29%. For a 50-50% mixture, CALIBRATION CURVE II is used instead.

2.5.3 Empirical Correlation of Mass Fraction of Plastic and Mixture Bulk Density

Empirical data has been collected to relate mass fraction of plastic and mixture bulk density for particles that are 212 μm or larger. Three sets of individual measurements on mixture bulk density were done on different mass fraction of plastic, whereby mass fraction of plastic was varied from 0% to 100% of the mixture. (Figure 2-16) The mass fraction was measured using a Setra EL-2000S two-decimal-digit precision digital scale while the volume was measured with a 10 ml pyrex graduated cylinder. Due to measurement error and the fact that particles do vary in size to a certain extent, there is a slight scatter of mixture density reading for a given mass fraction of plastic. Unfortunately, the mixture particle-particle void fractions are not known exactly. However, whenever a bulk density measurement is taken, the volume reading is read only after tapping is done and volume changes no further. This ensures that the particles are packed in the smallest volume possible. This criterion is consistent for all bulk density measurements. A linear curve fit was used to correlate the mass fraction of plastic and the corresponding mixture density. A linear curve fit is appropriate since mixture bulk density is expected to be linearly proportional to the mass fraction of plastic. An error estimation will be given in the next section. Experimental measurements of mixture bulk density and mass fraction of plastic/cork are given in Appendix C for CALIBRATION CURVE I and II.

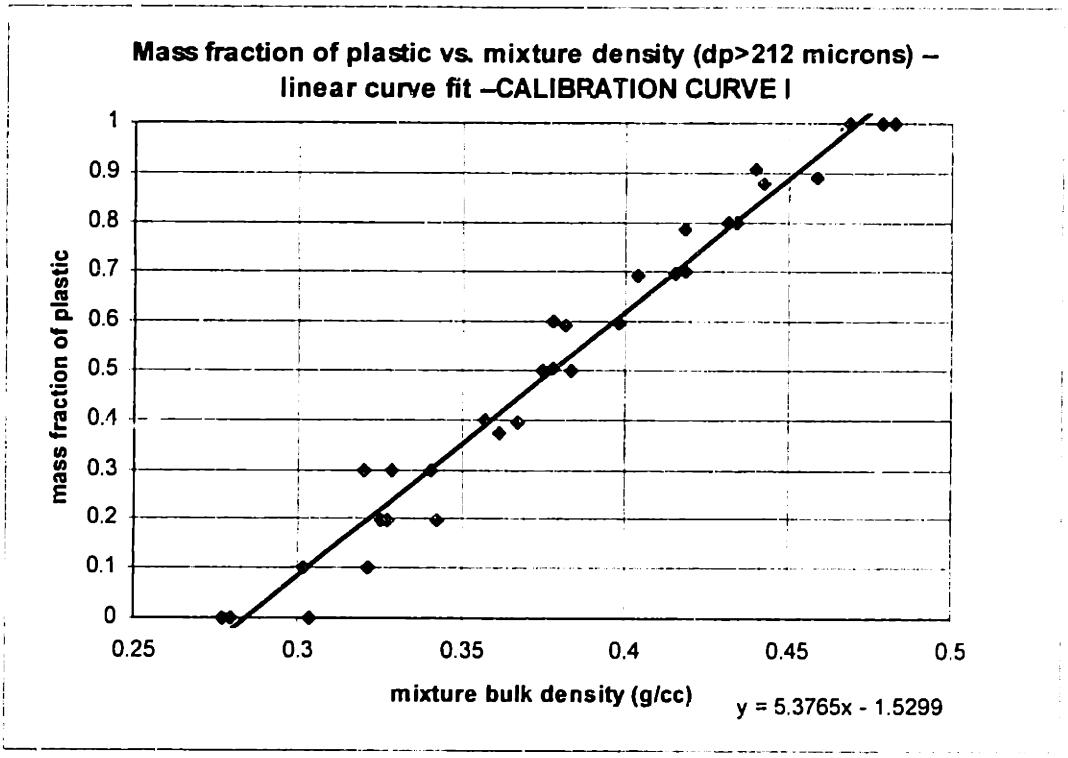

PSD of plastic particles used for CALIBRATION CURVE I	
size range (μm)	frequency (%)
212-355	78.5
355-500	19.2
500 and above	2.3

Calibration curve I is suitable for a 25% plastic -75% cork mixture as can be seen by the PSD results in Chapter 3.

Figure 2-16 CALIBRATION CURVE I - Empirical data on mass fraction of plastic and mixture bulk density

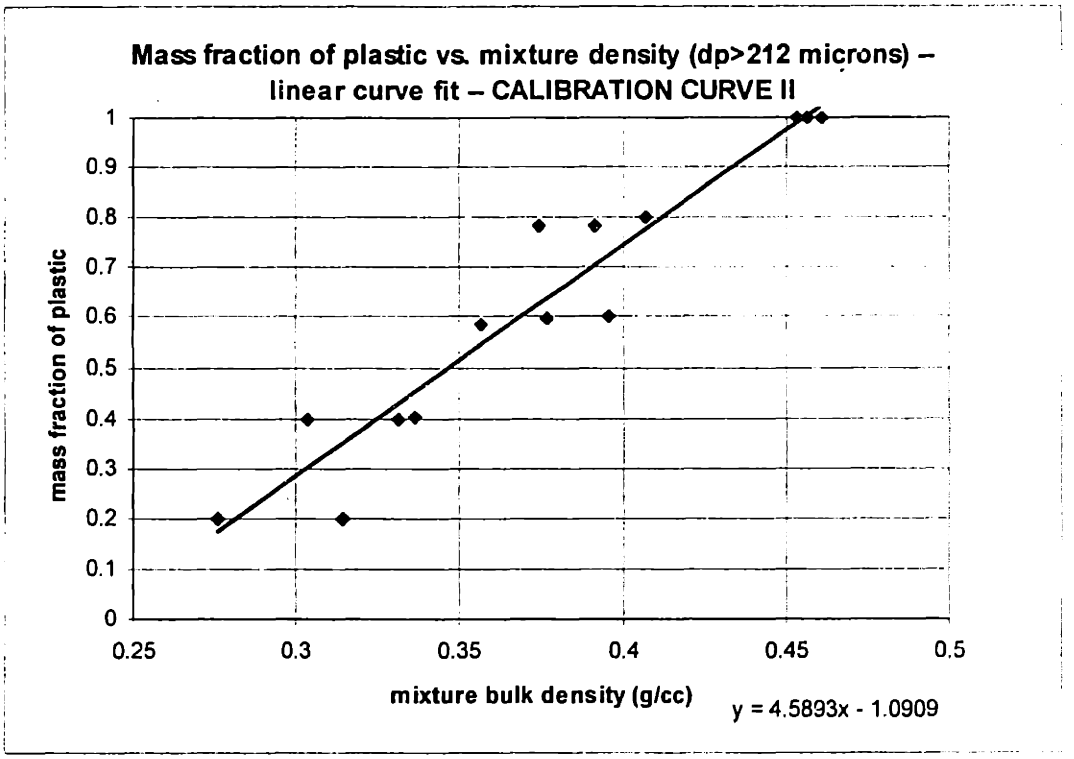

PSD of plastic particles used for CALIBRATION CURVE II	
size range (μm)	frequency (%)
212-355	37.4
355-500	21.9
500-710	21.6
710-1000	9.5
1000-1400	9.6

Calibration curve II is suitable for a 50% plastic -50% cork mixture as can be seen by the PSD results in Chapter 3.

Figure 2-17 CALIBRATION CURVE II - Empirical data on mass fraction of plastic and mixture bulk density

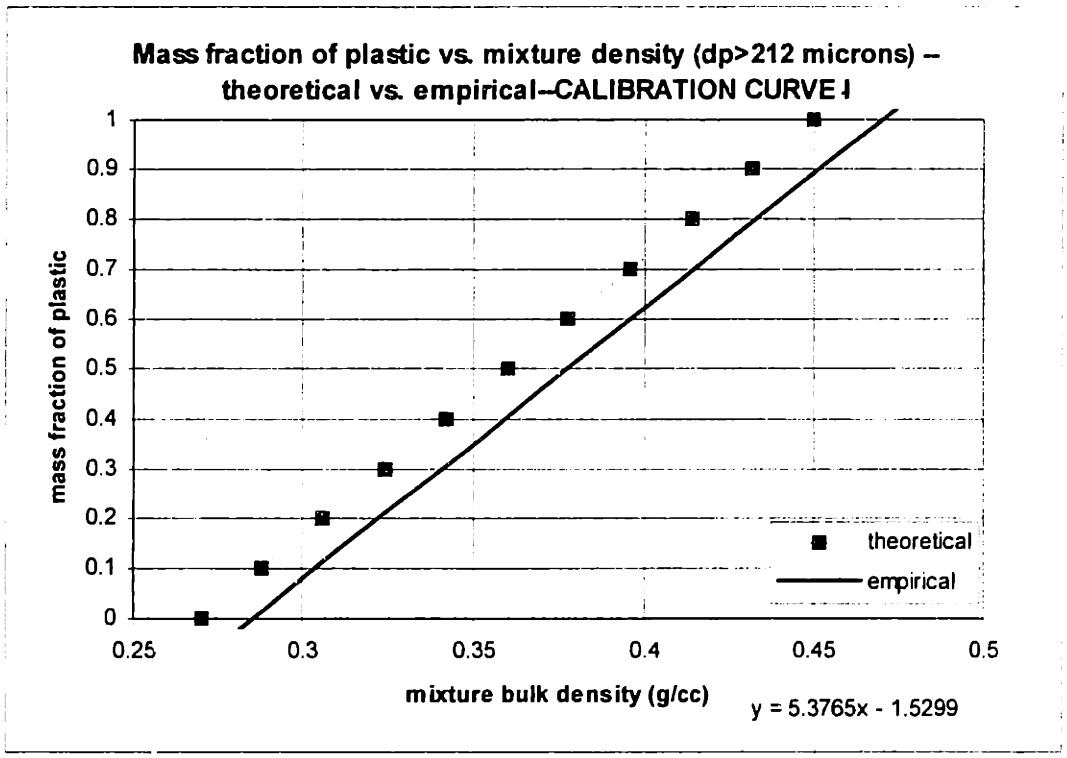

Figure 2-18 Comparison of Plastic Mass Fraction Calibration Curves - Empirical and Theoretical

2.5.4 Uncertainty Analysis

A digital scale (Setra EL 2000s) with a precision of two decimal places and a measuring cylinder of capacity of 10 cm^3 with markings to the nearest 0.1 cm^3 were utilized for the measurement of mass and bulk volume respectively of mixture. Errors in mass measurement of solid samples are in the range of $\pm$ 0.01 g while errors in bulk volume measurement are $\pm$ 0.1 cm^3. By keeping the mass and bulk volume used in the measurement much larger than their respectively uncertainty errors, error in bulk density measurement can be reduced.

A typical case would have a nominal mass of 2 g (~ 200 times of uncertainty of 0.01g) and a nominal bulk volume of 6 cm^3 (~ 60 times of uncertainty of 0.1 cm^3). The maximum bulk density error range would be $\pm$ 2.2%. If both nominal mass and bulk

volume values are reduced to half, the density error resulted would be doubled to ± 4.48%. It can be seen that density measurement error can be reduced by increasing the amount of solid sample measured.

Figure 2-16 consists of three sets of measurement of bulk density for given mass fractions of plastic particles. A linear fit was performed on the data using the least square method. The linear fit has the form of $X_p = 5.3765\ \rho_{bulk,\ mixture} - 1.5299$ (where X_p is the mass fraction of plastic). Assuming that data points satisfy the normal Guassian distribution, the calculated standard deviation, σ is **0.0556** with a maximum deviation of 0.113. Thus for a given mixture density, it is reasonable to assume that there is a 66.67% chance that the mass fraction of plastic will be within a ± σ (0.0556 or 5.56%) from the mean. Figure 2-19 is a repeat of Figure 2-16 with the addition of standard deviation error limits.

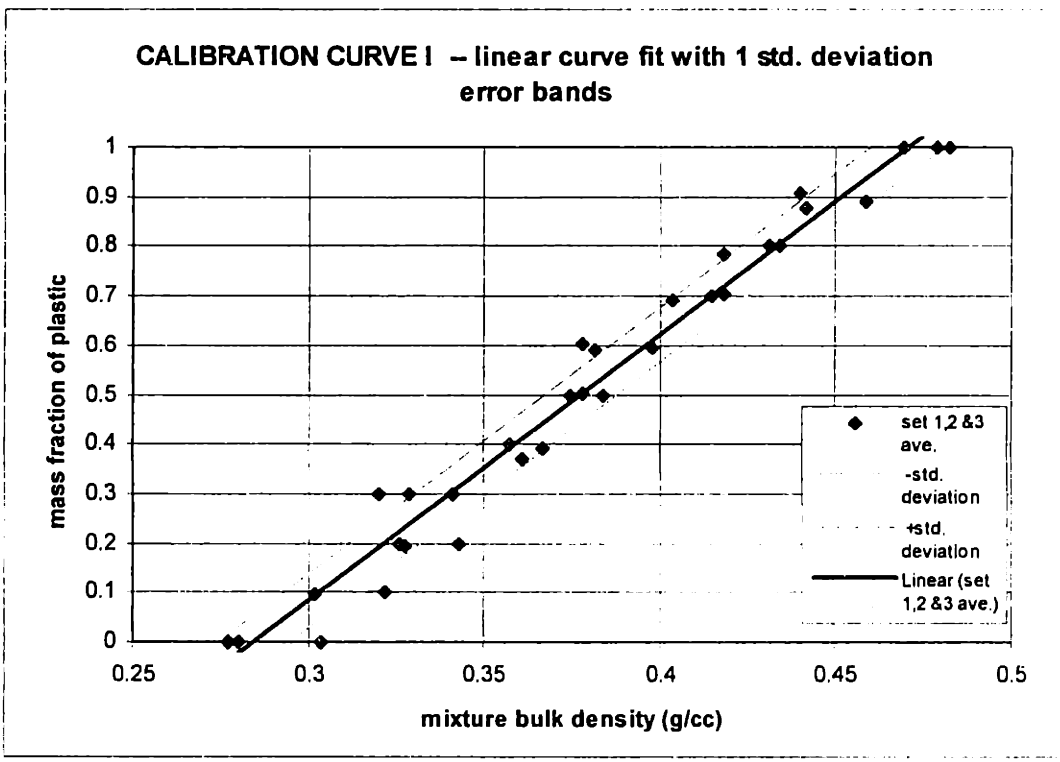

Figure 2-19 Experimental Correlation of Mass Fraction of Plastic and Mixture Bulk Density with Error bands

Uncertainty in the probe tip suction velocity can be estimated from the uncertainty in rotameter reading. The rotameter reads to the nearest 0.5 LPM (liter-per-minute). With an average cross section area of 2.92 e-5 m^2 at the probe tip, an uncertainty of 0.5 LPM corresponds to a local probe velocity of 0.29 m/s. At a U_o of 2 m/s, the uncertainty local probe velocity is approximately 14.5%.

2.5.4.1 Error Estimates for Negligence of Smaller Plastic Particles

It can be seen from Table 2-4 that 26.7% of plastic particles in the original mixture are smaller than 212 μm. For simplicity of approximation, let's assume that the plastic PSD in a given sample is identical to the original mixture. For a given sample, let m_p = estimated mass of plastic larger than 212 μm using the appropriate calibration curve; let m_c be the total mass of cork; the total mass of the mixture is thus m_p+m_c.

Again for this given sample, if 26.7% of plastic is < 212 μm, the true total mass of plastic in this sample is $1.267m_p$ instead of just m_p. Thus, the mass fraction of plastic including the particles below 212 μm is $x_{p,\,all} = \frac{1.267 m_p}{m_p+m_c}$, and the change in mass fraction of plastic, $\Delta x_p = x_{p,all} - x_p$. For a typical case, m_p is 12.6 g and m_c is 27 g and $x_p = 0.32$. The total mass of mixture is 39.6 g. $x_{p,all} = \frac{1.267(12.6)}{39.6} = 0.403$, and $\Delta x_p = 0.08$ or 8%.

Therefore, with the current assumption that plastic smaller than 212 μm are neglected, the mass fraction of plastic is underestimated by about 8% for a typical case.

2.6 Instrumentation - Variable Measurement

This section describes measurements for the MIT lab scale cold model. Airflow measurement for superficial gas velocity; solid recirculation rate; and pressure signals from pressure transducers will be discussed here.

2.6.1 Airflow - Measurement of Superficial Gas Velocity

A concentric-bore square edged orifice of bore diameter 2.094" placed upstream of the distributor is used for the measurement of air flow rate. The pipe upstream of the orifice is 4" in I.D. and is at least ten pipe diameters long. Piping immediately downstream of the orifice is also 4" I.D. Flange taps were used to measure the pressure drop across the orifice plate. The pair of pressure taps were connected to an inclined oil manometer which was used to read pressure drop. The manometer has units scaled to inches of water and utilizes red gage oil which has a specific gravity of 0.85. The supplier is Dwyer Instruments.

Calculations from pressure drop across orifice plate to volumetric flow rate in the pipe require also the compressed air temperature and the upstream gage pressure. Once volumetric flow rate is known, calculation of superficial gas velocity in the riser is straight forward. Procedures can be found in standard fluid flow measurement handbooks such as Flow Measurement Engineering Handbook by Miller (1983) and Mechanical Measurements by Beckwith, Marangoni and Lienhard (1993).

2.6.2 Solid Recirculation Rate - Flux

Markings along the transparent side wall of the return leg depicts a known distance, H in which an assumed plug flow travels during a test run. By monitoring the descent of particles along the return leg and keeping track of the required time, solid recirculation rate can be calculated with an estimated average mixture bulk density, $\rho_{bulk,\,mix}$. $\rho_{bulk,\,mix}$ is estimated using $x_p\,\rho_{bulk|\,p} + x_c\,\rho_{bulk|\,c} = \rho_{bulk|\,mix}$ where $\rho_{bulk|\,p}$ can be estimated between 0.45 - 0.50 g/cc while $\rho_{bulk|\,c}$ is approximately 0.203 g/cc. For the case with 25% cork-75% plastic, x_p is 0.25 while is x_c 0.75. For the case with 50% cork-50% plastic, both x_p and x_c are 0.5. It must be noted that this is a very crude approximation for dissimilar solids since the actual composition entrained and being recycled does vary from the initial mixture composition. Sample study does show that there is less coarse (plastic) being entrained at a given velocity.(Figure 3-10 & Figure 3-11) It's been observed that at any

given flux, x_p at the exhaust of the primary cyclone is in the range of 10 to 12%. Thus the actual $\rho_{bulk|\ mix}$ will be lower than the estimation. The table below illustrates the differences in $\rho_{bulk|\ mix}$ between original mixtures and steady state entrained sample measurements in the return leg in the cold model.

Mixture (original composition)	$\rho_{bulk\|\ mix}$ original mix. [kg/m^3]	G_s [kg/m^{2}s]	$\rho_{bulk\|\ mix}$ entrained mix. [kg/m^3]	G_s [kg/m^{2}s]
25% plastic 75% cork	277	1.62	238	1.43
25% plastic 75% cork	277	5.75	236.6	5.04
50% plastic 50% cork	327	4.6	241	3.13
50% plastic 50% cork	327	7.2	237	4.8

Table 2-7 Comparison of Mixture Bulk Densities - original mixture and entrained mixture

For a 25-75% mixture, $\rho_{bulk|\ mix}$ of entrained solids is about 14% lower than that of the original solids. For a 50-50% mixture, it is about 27%. The corresponding G_s are affected as well. Figure 2-20 shows the setup for measurement of solid flux during operation and this technique requires a plug flow assumption in the return leg.

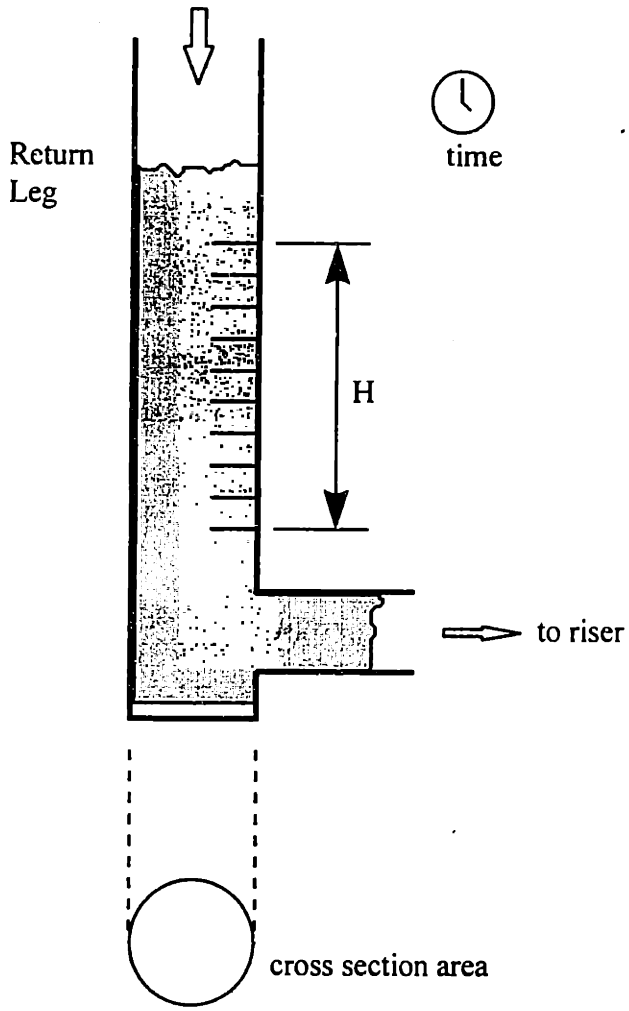

Figure 2-20 Solid Recirculation Rate Measurement Technique

The return leg is also equipped with a butterfly valve which can be shut temporarily while an air bypass is left open during operation so that the solid pile up rate can be observed. The solid pile up rate can be translated into solid recirculation rate. According to Hyre (1995), the two techniques mentioned above were seen to yield similar results. The butterfly valve technique yielded a standard deviation from the average time to drop a given distance is between 2 to 5 %. The visual descent technique gave a standard deviation of 3 to 5 % of the average value. A comparison of the two methods and details of the solid-pile-up method can be found in Hyre Chapter 2 Section 4.5.2 (1995).

For low density particles such as granulated cork, it has been observed that slight fluidization does occur even in the return leg after a fraction of the particles are

transferred into the riser. This prevents the assumption of plug flow in the downcomer to be accurate. Thus, a more accurate method of predicting solid recirculation rate in the current configuration is by the butterfly valve technique. This technique was utilized for all cases run.

2.6.3 Pressure Measurement - Pressure Transducer

Pressure measurements along the riser at various locations can be related to the volumetric solid fraction profile. The shape of a solid fraction profile is an indication of the characteristic hydrodynamic behavior of particles in the system. Volumetric solid fraction, 1-ε (where ε is the void fraction) is related to pressure drop ΔP across a distance h by the following hydrostatic equation: (where acceleration effects, viscous effect near the wall and the particle free fall are negligible.)

$$\Delta P = (1-\varepsilon)\, \rho_s g h$$

Pressure measurements in the MIT cold model are made by pressure transducers supplied and calibrated by AutoTran, Inc (series 600). There are altogether 7 pressure taps along the riser and they are connected to 6 pressure transducers through 1/8" diameter flexible tubing. The length is each tubing is minimized to prevent signal attenuation. The exact locations of the taps were shown in Figure 2-14 . The taps cover a dimensionless bed height from 5% to 75%. All transducers require an input of 12 V DC and produce an output of 1-5 V. The bottom three transducers have a rated pressure range of -1 to 10 inches of water column (WC) while the top three have a range of -1 to 5 inches of WC. Their calibrations are given in APPENDIX D.

The pressure taps are angled down into the bed to prevent particle build-up near the wall at the entrance of the tap based on the assumption of core-annulus flow model. The angle is 40°. However, it was found that having an angle near the wall was not sufficient to keep the taps, especially the ones near the bottom, clear of particle build-up. Purged air

was employed to keep the bottom taps clear. The setup of two typical taps with purged air is as followed:

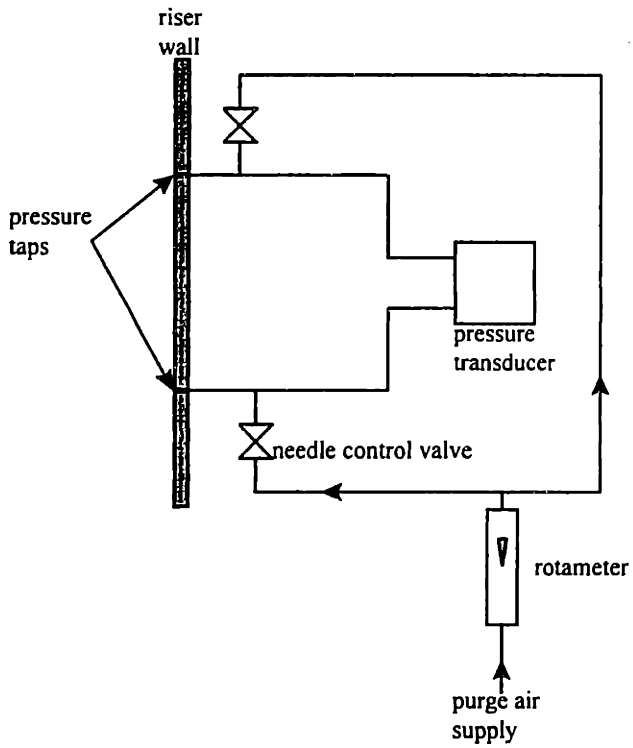

Figure 2-21 Purge Air / Pressure Tap Setup Schematic

The purge air is turned off during the period of time in which pressure signals are being taken and recorded. This eliminates the step of re-calibrating the transducers with the presence of purge air and allows a simple rotameter to control the purge air flow rate. The period is approximately 10 seconds. Purge air is useful especially in keeping the taps clear from particles during the times before pressure signal is recorded. After the signal is taken, purge air is introduced back into the taps by opening the needle control valves.

Although seven taps were built on the wall of the riser, the bottom one is not useful in predicting the solid induced pressure drop. Due to geometry of the distributor and the jet like exit of fluidizing gas, there is an entrance effect forming an acceleration zone near the bottom of the riser. This zone has been both modeled analytically using a momentum

conservation control volume and measured experimentally using the existing pressure taps near the bottom. The results are presented in the next section.

2.6.3.1 Acceleration Zone - near bottom of bed

To understand the physics and to approximate the negative pressure drop, the acceleration zone near the bottom of the bed can be modeled using the linear momentum theorem. A control volume is drawn for that section of the riser and is shown in Figure 2-22 . Note that there is no air flow at the bottom of the riser except through the jet.

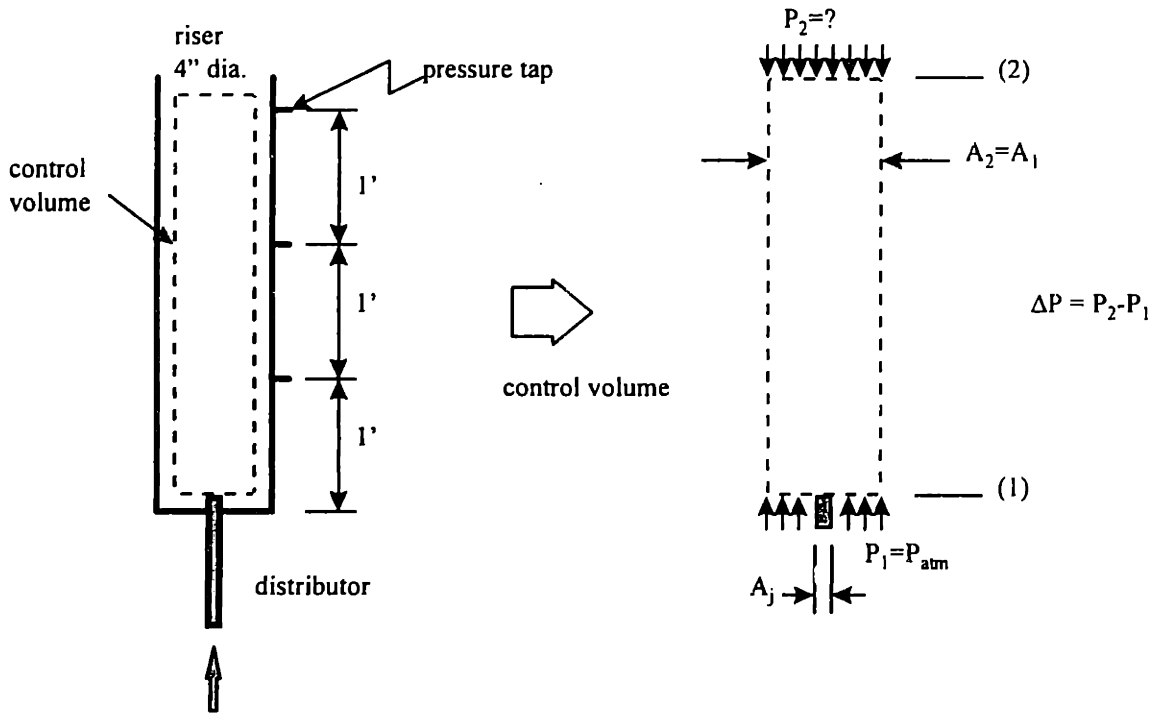

Figure 2-22 Control Volume of the Bottom Region of the Riser

The linear momentum theorem can be simplified to the following force balance equation on the control volume. For simplicity of analysis, gravitational and viscous effects are neglected. Gravitational forces even with particles are small when compared to the

pressure force term and they are presented below. Flow can be approximated as incompressible as followed:

$$\dot{m}V_2 - \dot{m}V_j = (P_j A_j + P_1 A_1) - P_2 A_1 - m_{particle} g$$

where air mass flow rate, $\dot{m}$ is the same for section 1 and 2. A_j is the cross section area of the jet and is negligible compared to A_1 ($A_1/A_j = 28.4$ or $A_1 >> A_j$). V_j is the jet exit velocity into the control volume while V_2 is the superficial gas velocity for the entire bed cross section. At the jet exit, $P_1=P_j$.

$m_{particle}$ is the mass of particles in the acceleration zone and can be estimated from approximated values of solid fraction in the zone. A typical volumetric solid fraction, $1-\varepsilon$ near the bottom of the bed is in the vicinity of 2 %. The volume of the acceleration zone can be calculated by A_2H where H is the distance from the distributor to the 3rd pressure tap and the value is 3.0' (0.914 m). A_2 from Table 2-8 is 0.0081 m^2. Thus volume occupied by solid in this zone is simply $(1-\varepsilon)(A_2H)$. $m_{particle}$ in this zone is $(1-\varepsilon)(A_2H)\rho_{solid,\ mixture}$ where $\rho_{solid,\ mixture}$ is the solid mixture density. $\rho_{solid,\ mixture}$ for a 25% plastic-75% cork mixture is calculated using $x_p\rho_{solid|\ p} + x_c\rho_{solid|\ c} = \rho_{bulk|\ mix}$ where x_p is 0.25 and x_c is 0.75. Substituting the above correlation with appropriate values yields $m_{particle}$ = 0.04 kg. Thus $m_{particle}$ g is 0.40 N. $(\Delta P_2)A_2$ is calculated to be around 1.39 N. $\Delta P_2 A_2$ is about 3 times larger than $m_{particle}g$ but is of the same order of magnitude. Thus for estimation of pressure drop near the bottom of the riser, it is best to include the gravitational term in. The linear momentum equation becomes:

$$\dot{m}V_2 - \dot{m}V_j = P_1 A_1 - P_2 A_1 - m_{particle} g$$

With a $m_{particle}g$ of 0.40 N and an assumption of 2 % average solid fraction within the first 3 feet of the riser, $\Delta P=P_2-P_1$= 99.1 N. There is still a negative pressure drop in the bottom even with particles. However, the effect is more obvious without particles.

The negative pressure drop with no particles has been both measured and estimated using the linear momentum theorem at two superficial gas velocities, U_o= 1.6m/s and U_o= 2.0m/s. Estimated and measured pressure drop values with no solid recirculation are compared in Table 2-8

	U_o = 2 m/s	U_o = 1.6 m/s
$\dot{m}$ [kg/s]	.02095	.01592
V_j [m/s]	59.54	45.26
V_2 [m/s]	2.095	1.6
$A_1 = A_2$ [m^2]	.0081	
A_j [m^2]	2.85e-4	
$P_1 = P_{atm}$ [Pa]	1.0133e5	
$\Delta P = P_2 - P_1$ [Pa] estimated using control volume with no particles	**148.6**	**85.81**
$\Delta P = P_2 - P_1$ [Pa] measured with no particles	**172**	**126.6**

Table 2-8 Tabulated Values for Acceleration Zone Pressure Drop (measured and estimated without particles)

The pressure increase values from section (1) to (2) of the control volume agree reasonably well with the measurement for the two cases with different superficial gas velocities. The result of this approximation shows that pressure readings near the bottom of the bed are unreliable in predicting a solid fraction especially when the superficial gas velocity is high. It has been observed from the differential pressure measurement that the next (4^{th}) pressure tap up from the distributor does not exhibit any acceleration effect and that there is a positive pressure drop between the 3^{rd} and the 4^{th} pressure tap. This suggests that the acceleration zone ends between the 2^{nd} and the 3^{rd} pressure tap. Since the distance from the distributor to the 3^{rd} pressure tap is 3', it is reasonable to estimate the acceleration zone height between 2' and 3' from the distributor or approximately 2.5'. This value can be confirmed by the simple turbulent free jet model.

The jet exiting the distributor is approximately at 2m/s and can be considered as a free turbulent jet as the Reynold's number, $Re_D \approx 2500$ or just in the vicinity of the transition zone and that $A_{riser} >> A_{jet}$. Let r be the jet radius which is measured from the centerline of the jet to the locus of fluid velocities one-half those at the centerline of the jet; and let the jet angle, θ be the half-angle of the cone formed by the locus of the half centerline

velocities. For free turbulent jets the half angle is found to be about 5°. (Davies, 1972) This model estimates that 45% of the total volumetric flow is within the half-speed cone. The outer limit of the jet is less well defined and can be approximated using a 10° half-angle cone.

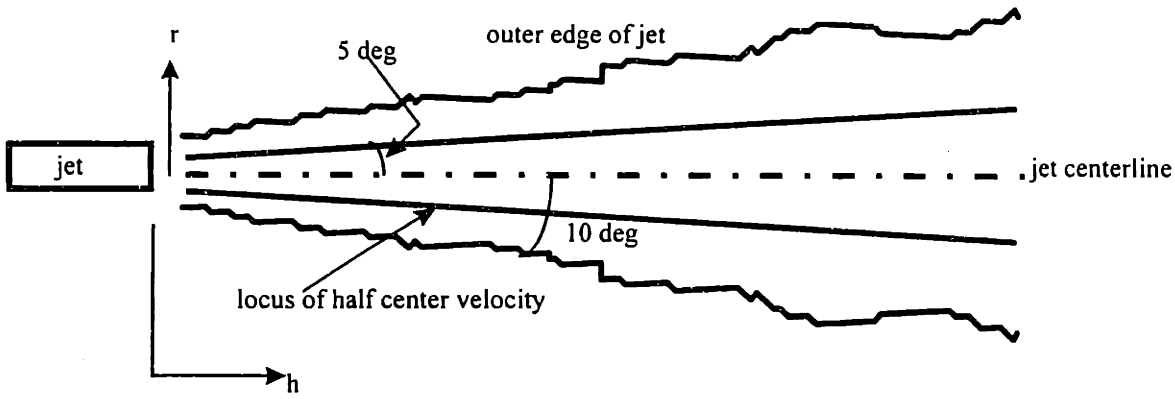

Free turbulent jet

Figure 2-23 Free Turbulent Jet Schematic

Using the half-centerline velocity angle 5° and setting the locus of the half centerline velocity equal to the riser bed radius of 2" or 0.0508 m yields an acceleration zone height of 0.581 m or 1.91 ft (from the distributor). This estimated acceleration zone height of 1.91 ft is close to the average distance between the 2nd and the 3rd pressure tap, which is 2.5 ft.

2.6.4 Uncertainty Analysis

Various sources of error are introduced into the variable measurement process and their presence will affect each category of measurement listed in this section. Airflow measurement error can affect the superficial gas velocity; an error in estimating the descent speed of particles in the return leg can affect the solid recirculation rate; and an error in differential pressure measurement can affect the volumetric solid fractions in the riser. In order to understand the influence of these errors on variable measurements, Hyre

(1995) has performed a series of analysis on variable measurement errors. Details of his error analysis can be found in Hyre (1995) Chapter 2 Section 4.5.

Fluctuation of compressed air supply can affect the superficial gas velocity. The pressure drop across the square-edge orifice plate has been measured by an inclined manometer. Fluctuations of pressure from 0.01" to 0.02" of Water Column have been observed at times.

Solid recirculation measurement using both butterfly valve technique and visual descent technique were compared at a given flux. Time to travel 2 inches in the downcomer were repeated and recorded for ten times; the averages are as followed:

	Valve technique (time to travel 2")			Descent technique (time to travel 2")		
Flux	high	medium	low	high	medium	low
average[s]	3.24	4.09	5.09	3.07	4.11	4.97
Std. Dev.	0.157	0.146	0.0932	0.147	0.140	0.134

Table 2-9 Solid Recirculation Measurements - visual and descent technique[10]

Pressure signals were taken repeatedly during a test run at a frequency of 100 Hz for 8 sec after the bed had reached steady state. The pressure signals were then averaged to calculate the solid fraction profile. The standard deviation from the mean time varying signals were given which can be used to estimate the error involved in the mean pressure reading.

[10] Taken from Hyre (1995) Chapter 2 Section 4.5.2 P 189

2.7 Data Acquisition

A Gateway Pentium-66 PC together with a data acquisition board (DAS-1601 from Keithley-Metrabyte) were the necessary hardware needed for the measurement of the time-varying pressure transducer signal. Software used was Easyest LX and was supplied by Keithley-Metrabyte also. DAS-1601 is a 12-bit high speed D/A board that can measure 16 time-varying signals simultaneously. Six of the sixteen channels on the D/A board have been used for the six pressure transducers at a sampling frequency of 100 Hz. The sampling frequency for a cold bed has been investigated by Westphalen (1990). The setup of the MIT cold model data acquisition system is shown in Figure 2-24 . With the pressure calibration curves installed into the Easyest LX software, the voltage output of the pressure transducers can be converted directly into pressure drop in either cm of Water Column (WC) or inches of WC.

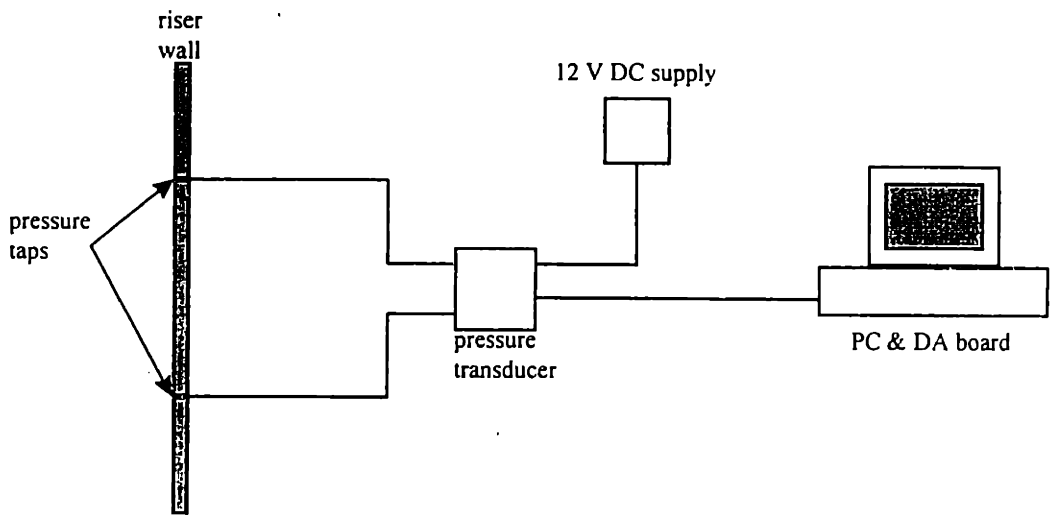

Figure 2-24 Setup of Data Acquisition System

3. Results and Discussion

As mentioned in Chapter One, parameters such as solid fraction profiles, mass fraction of each of the dissimilar materials and their corresponding particle size distributions at a given bed elevation can give an insight to the hydrodynamic behavior of a fluidized bed. This chapter thus presents these parameters for a given set of operating conditions.

3.1 Cold Model Test Matrix

The table below is a summary of the cold model operating conditions.

Cold Model					Corresponding Hot Bed				
mixture	U_o [m/s]	Fr = U_o^2/gD	G_s [kg/m^{2}s]	$G_s/\rho_s U_o$	mixture	U_o [m/s]	Fr = U_o^2/gD	G_s [kg/m^{2}s]	$G_s/\rho_s U_o$
25% plastic 75% cork	2	4.02	1.62	0.00199	25% sorbent 75% char	2.65 (8.7 ft/s)	4.02	5.24	0.00199
25% plastic 75% cork	2	4.02	5.75	0.00705	25% sorbent 75% char	2.65 (8.7 ft/s)	4.02	18.56	0.00705
50% plastic 50% cork	2	4.02	4.6	0.0040	50% sorbent 50% char	2.65 (8.7 ft/s)	4.02	14.97	0.0040
50% plastic 50% cork	2	4.02	7.2	0.00627	25% sorbent 75% char	2.65 (8.7 ft/s)	4.02	23.43	0.00627

Table 3-1 Cold Model Test Matrix [11]

[11] ρ_s for a 25% plastic 75% cork mixture is 408 kg/m^3. For the hot bed, ρ_s for a 25% spent sorbent 75% char mixture is 994 kg/m^3. ($\rho_{s,sorbent}$ is 2243 kg/m^3 and $\rho_{s,char}$ is 577 kg/m^3)

3.2 Steady State Time Effect

In order to properly simulate the steady state hydrodynamic behavior of the pilot plant, it is essential to understand the amount of time needed by the cold model to reach steady state. One of the parameters that can easily be measured and can accurately reflect the steady state effect is the differential pressure drop caused by solid particles. The measured differential pressure drop at all locations of the riser should remain constant once steady state is reached.

The differential pressure drop has been measured using the existing set of pressure transducers at a superficial gas velocity of 2 m/s and a solid recirculation rate of approximately 5.5 kg/m^2s with a 25% plastic-75% cork mixture. The result is shown in Figure 3-1 . PT 1 stands for Pressure Transducer 1 and is the bottom most transducer while PT 5 is the top most transducer in the riser. The negative pressure drop measured by pressure transducer 1 can be accounted for by the acceleration effect introduced in Section 2.6.3.1. It is obvious that pressure drop measurements are not steady at the first 70 seconds after the recirculation has begun. From approximately 70 to 150 seconds, there seems to exist a transition where the measurements are more stable than before. Beyond 150 seconds, pressure drop readings settle quite well and the system can be assumed to have reached steady state. For a case with lower solid flux, it is believed that a lesser amount of time is required to reach steady state. Data presented in the later sections were all measured at or after 150 seconds or 2 ½ minutes after turning on the L-valve

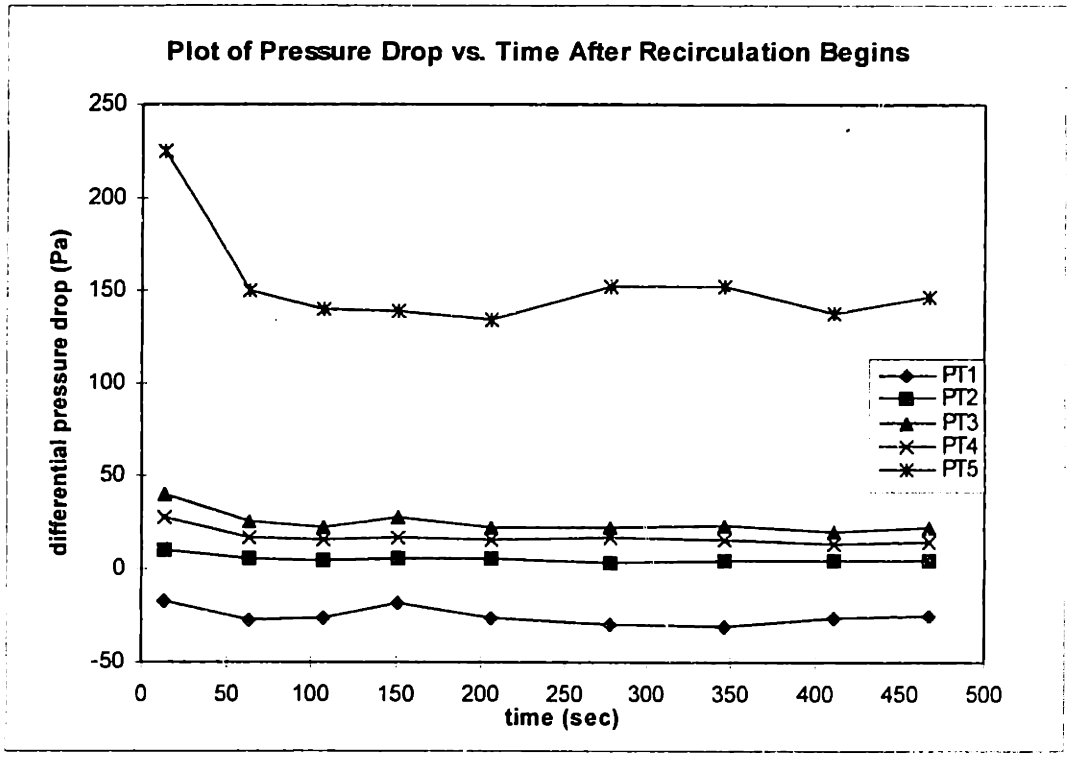

Figure 3-1 Effect of Differential Pressure Drop in the Riser as a Function of Time.

3.3 Solid Fraction Profiles

As described in Section 2.6.3, the solid fraction can be related to the differential pressure drop over a distance h by the following hydrostatic equation where acceleration effects, viscous effects near the wall and particle free fall are negligible.

$$\Delta P = (1-\varepsilon)\, \rho_{s,local}\, gh$$

where $\rho_{s,local}$ is the local solid density as determined by sample measurements. A more accurate estimation of the local solid fraction can be obtained from $\rho_{s,local}$ rather than an average solid density ρ_s as calculated from the original mixture composition. A local solid density profile can be constructed from a discrete set of density measurements from the various sample port locations. Table 3-2 summarizes the experimentally determined local solid density for all cold model test runs. Values between any two discrete points can be interpolated linearly. The calculation of solid fraction profiles were based on interpolation of values from this table.

	25-75% mixture U_o=2 [m/s] G_s=1.62 [kg/m^{s}s]	25-75% mixture U_o=2 [m/s] G_s=5.75 [kg/m^{s}s]	50-50% mixture U_o=2 [m/s] G_s=4.6 [kg/m^{s}s]	50-50% mixture U_o=2 [m/s] G_s=7.2 [kg/m^{s}s]
bed height (%)	$\rho_{s,local}$ [kg/m^3]	$\rho_{s,local}$ [kg/m^3]	$\rho_{s,local}$ [kg/m^3]	$\rho_{s,local}$ [kg/m^3]
16	410	505	483	566
37.2	426	446	487	507
56.4	512	512	513	504
72.3	449	490	458	569

ρ_s for a 25-75% mixture - 414 kg/m^3
ρ_s for a 50-50% mixture - 578 kg/m^3

Table 3-2 Local Solid Mixture Density at Different Operating Conditions - as determined by sample measurements

Due to the geometry of the distributor and its corresponding entrance region into the riser, there is the acceleration effect (as described in Section 2.6.3.1) which effectively makes the bottom of the riser an acceleration zone. Static pressure measurements in this zone are invalid. A comparison of the solid fraction profiles under different operating conditions are presented Figure 3-2 and Figure 3-3 . It can be seen that the solid concentration along the riser is a strong function of G_s. For both mixtures, an increase of G_s brings about an overall increase of solid concentration.

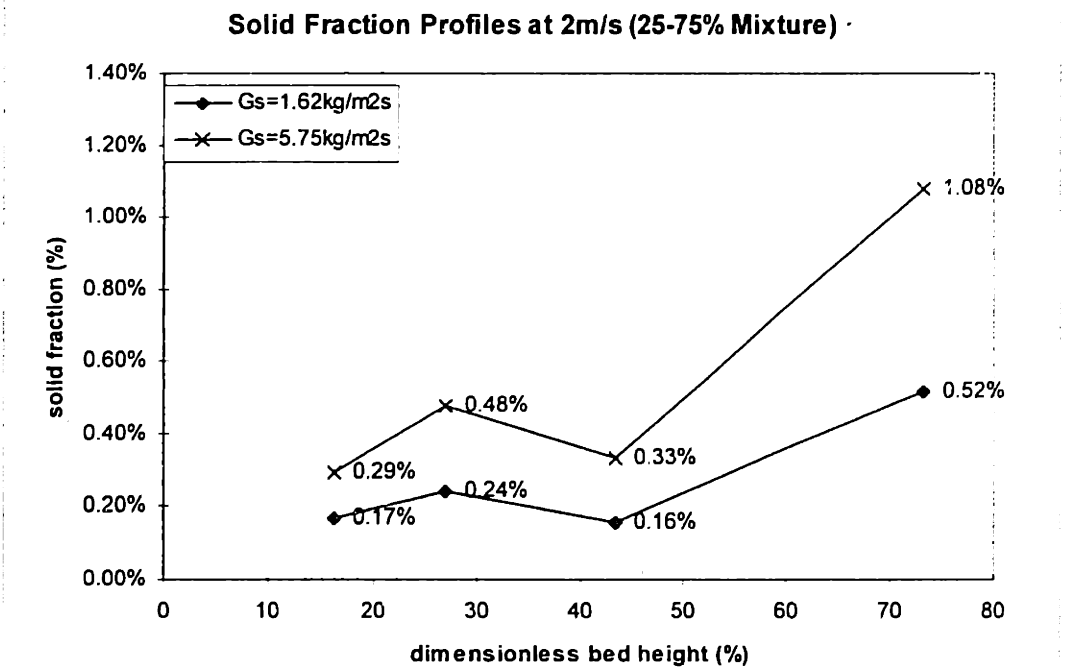

Figure 3-2 Average Solid Fraction Profiles for a 25-75% mixture at 2 m/s

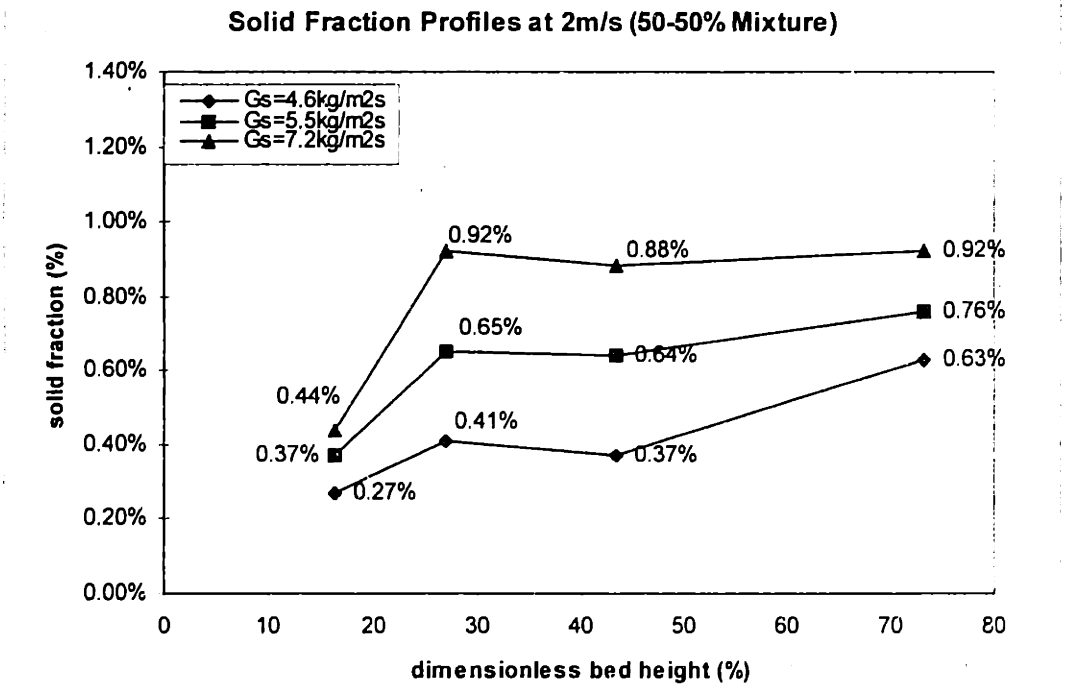

Figure 3-3 Average Solid Fraction Profiles for a 50-50% mixture at 2 m/s

Figure 3-4 to Figure 3-8 present the individual solid fraction profile at a given operating condition. The dotted lines represent locations of SP (Sample Port) and 'Vol.frac.(plastic)' represents the Volume Fraction of Plastic in the given locations. From the analysis of samples collected from the sample ports, the masses of both plastic and cork are known precisely. The volume of each material can be calculated by dividing its mass by its solid density. Knowing the total volume of both plastic and cork, the volume fraction of plastic can be calculated.

For example, sample analysis of SP1 in Figure 3-8 yields 18.60 g of plastic and 19.95 g of cork; knowing the solid density of plastic to be 0.905 g/cm^3 and that of cork to be 0.25 g/cm^3, the volume of plastic can be calculated by:

$$V_{plastic} = \frac{18.6g}{0.905\frac{g}{cm^3}} = 20.55\,cm^3$$

and volume of cork can be calculated by:

$$V_{cork} = \frac{19.95g}{0.25\frac{g}{cm^3}} = 79.8\,cm^3$$

Therefore, the total volume $V_{total} = V_{plastic} + V_{cork}$. Knowing the dimensionless solid fraction (1-ε) at that location from pressure measurement to be 0.44%, the volume fraction of plastic, $\overline{C}_{coarse}$ is thus,

$$\overline{C}_{coarse} = \frac{V_{plastic}}{V_{total}} \cdot 0.44\% = 0.09\%$$

The volume fraction of plastic is shown in the same figure to be 0.09% at SP1.

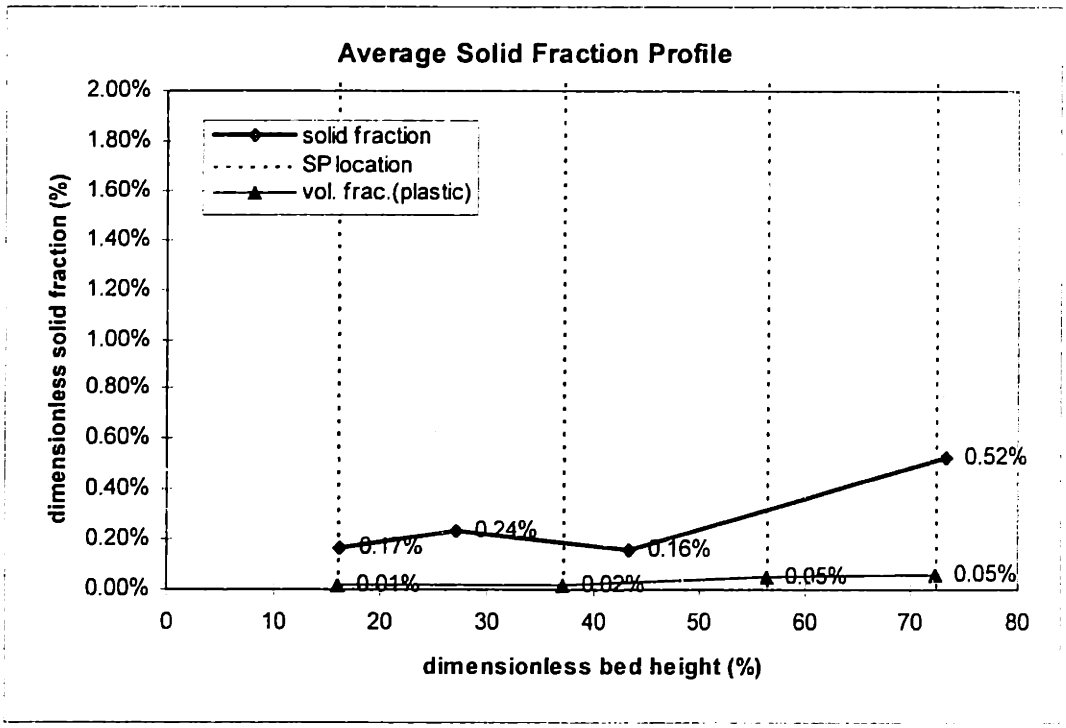

Operating Conditions		
	Cold Model	Corresponding Hot Bed
Solid Comp.	25% Plastic 75% Cork (by volume, 8.4% Plastic 91.6% cork)	25% Sorbent 75% Char
U_o [m/s]	2	2.65 (8.7 ft/s)
$Fr = U_o^2/gD$	4.02	
G_s [kg/m^{2}s]	1.62 (low)	5.24
$G_s/\rho_s U_o$	0.00199[12]	

Figure 3-4 Solid Fraction Profile - 25-75% mixture high velocity low flux

[12] ρ_s for a 25% plastic 75% cork mixture is 408 kg/m^3. For the hot bed, ρ_s for a 25% spent sorbent 75% char mixture is 994 kg/m^3. ($\rho_{s,sorbent}$ is 2243 kg/m^3 and $\rho_{s,char}$ is 577 kg/m^3)

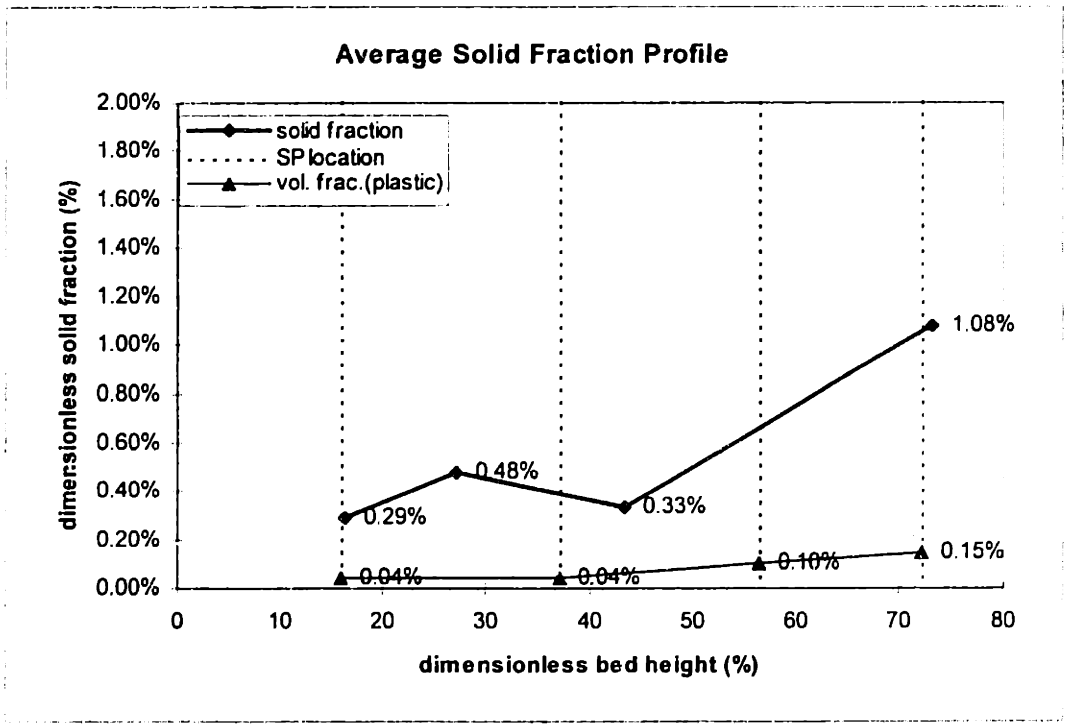

Operating Conditions		
	Cold Model	Corresponding Hot Bed
Solid Comp.	25% Plastic 75% Cork (by volume, 8.4% Plastic 91.6% cork)	25% Sorbent 75% Char
U_o [m/s]	2	2.65 (8.7 ft/s)
$Fr = U_o^2/gD$	4.02	
G_s [kg/m^{2}s]	5.75 (high)	18.56
$G_s/\rho_s U_o$	0.00705	

Figure 3-5 Solid Fraction Profile - 25-75% mixture high velocity high flux

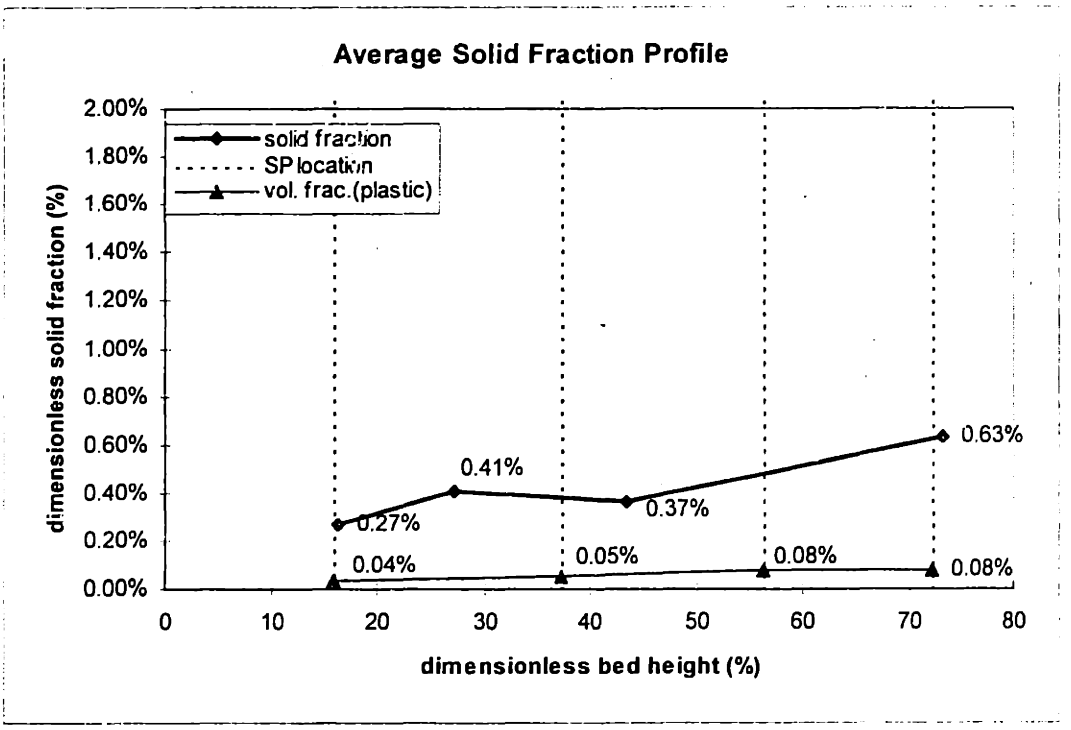

Operating Conditions		
	Cold Model	Corresponding Hot Bed
Solid Comp.	50% Plastic 50% Cork (by volume 21.6% Plastic 78.4% Cork)	50% Sorbent 50% Char
U_o [m/s]	2	2.65 (8.7 ft/s)
$Fr = U_o^2/gD$	4.02	
G_s [kg/m^{2}s]	4.6 (low)	14.97
$G_s/\rho_s U_o$	0.0040[13]	

Figure 3-6 Solid Fraction Profile - 50-50% mixture high velocity low flux

[13] ρ_s for a 50% plastic 50% cork mixture is 574 kg/m^3. For the hot bed, ρ_s for a 50% spent sorbent 50% char mixture is 1410 kg/m^3. ($\rho_{s,sorbent}$ is 2243 kg/m^3 and $\rho_{s,char}$ is 577 kg/m^3)

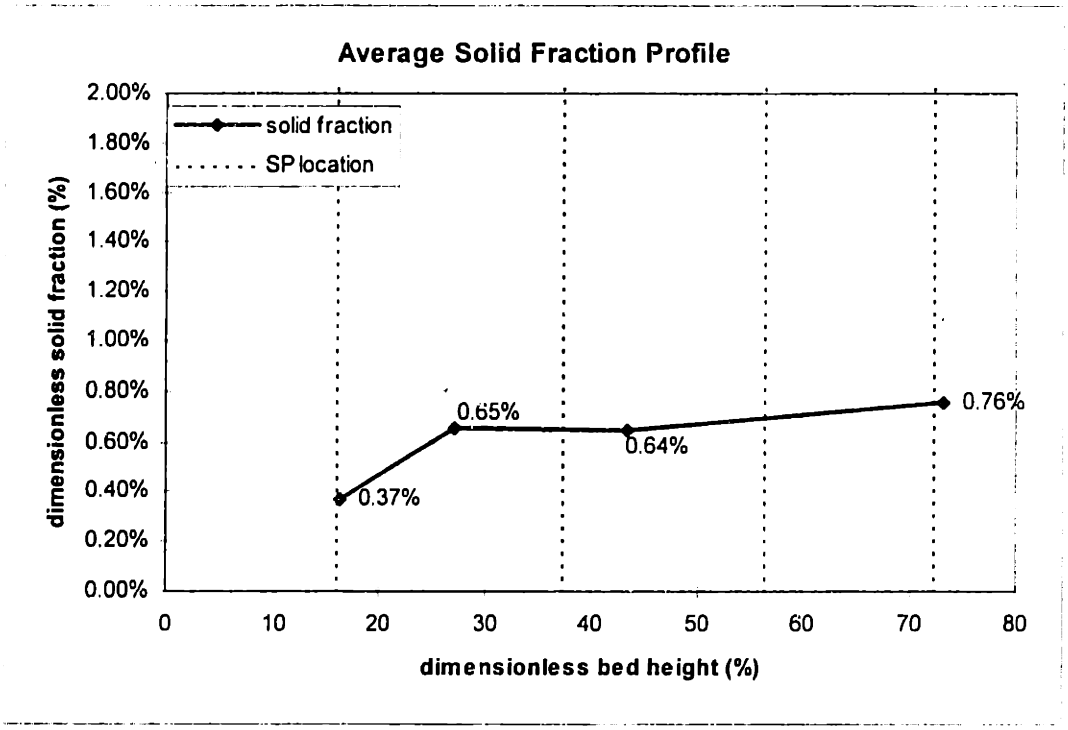

Operating Conditions		
	Cold Model	Corresponding Hot Bed
Solid Comp.	50% Plastic 50% Cork (by volume 21.6% Plastic 78.4% Cork)	50% Sorbent 50% Char
U_o [m/s]	2	2.65 (8.7 ft/s)
$Fr = U_o^2/gD$	4.02	
G_s [kg/m^{2}s]	5.5 (medium)	17.9
$G_s/\rho_s U_o$	0.00479	

Figure 3-7 Solid Fraction Profile - 50-50% mixture high velocity medium flux

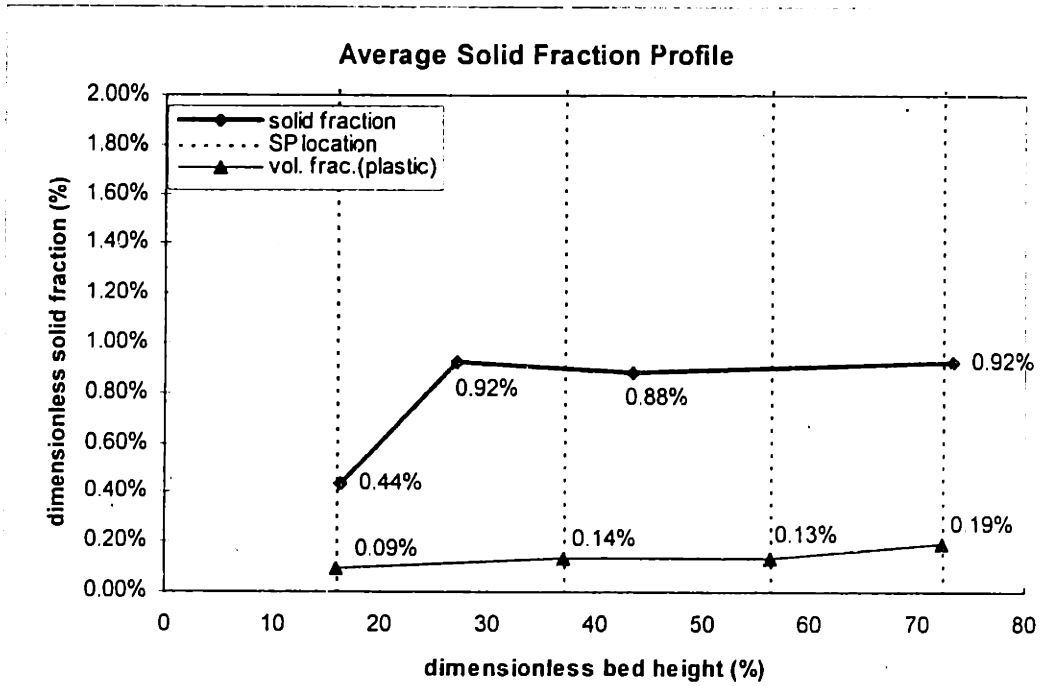

Operating Conditions		
	Cold Model	Corresponding Hot Bed
Solid Comp.	50% Plastic 50% Cork (by volume 21.6% Plastic 78.4% Cork)	50% Sorbent 50% Char
U_o [m/s]	2	2.65 (8.7 ft/s)
$Fr = U_o^2/gD$	4.02	
G_s [kg/m^{2}s]	7.2 (high)	23.43
$G_s/\rho_s U_o$	0.00627	

Figure 3-8 Solid Fraction Profile - 50-50% mixture high velocity high flux

A general trend for most of the solid fraction profiles, especially the ones with a low concentration of plastic show an increase of solid concentration near the top of the riser, in the range of approximately 72% dimensionless bed height. This phenomenon can be explained most appropriately by the extended abrupt exit geometry, as other investigators (Brereton and Grace (1994)) with a similar exit geometry experienced the same 'solid pile-up' near the top. The exit geometry of the cold model can be described as extended abrupt as shown in the following figure.

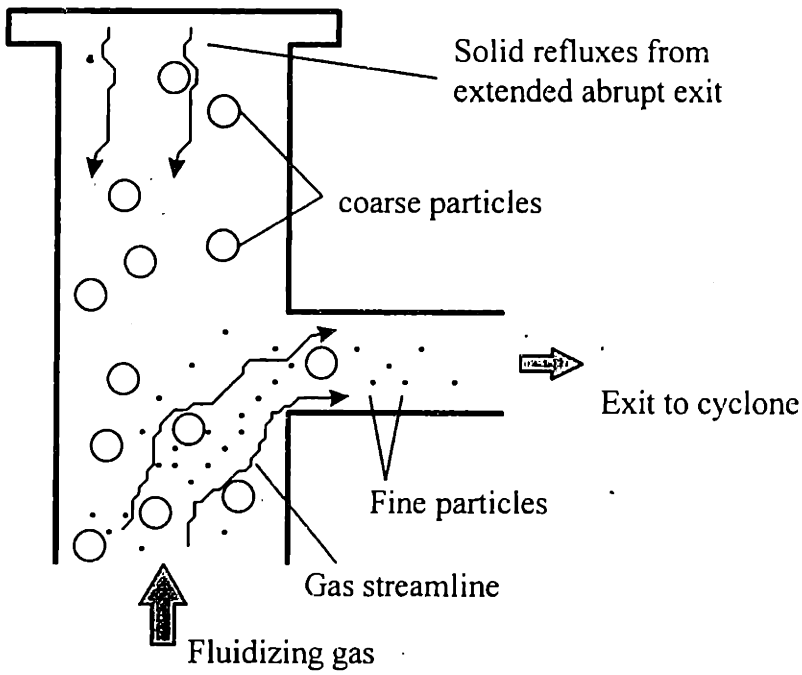

Figure 3-9 Extended Abrupt Exit Geometry

An abrupt exit geometry as such causes inertial separation, whereby the coarse has a tendency to be reflected back into the riser while the fines tend to follow the gas streamline and exit the riser.

Brereton *et al* (1994) investigated a number of abrupt exit geometries and their corresponding solid fraction profiles. Sand particles with a d_p of 148μm and $\rho_s \approx 2650$ kg/m^3 were fluidized in a riser with an extended abrupt exit. Various U_0 were used to fluidize the particles; the minimum and maximum of which exceed U_t of sand at

approximately three and nine times respectively. His results indicated that the solid fraction profile had a strong dependence on the exit geometry and U_o. With an extended abrupt exit and $\frac{U_o}{U_t} \approx 9$, the dimensionless solid fraction at approximately 90% dimensionless bed height was about a factor of three higher than that at 40% dimensionless bed height which had the minimum solid concentration. This 'reflux' effect extended down to approximately 60% dimensionless bed height.

The MIT cold model has an abrupt exit geometry identical to that of Brereton described above. With $\frac{U_o}{U_t} \approx 10$ (where U_t was calculated for plastic), a similar trend has been observed.

3.4 Mass Fraction of Coarse

The mass fraction of plastic, x_p (coarse) as a function of riser height is of primary interest. x_p's are plotted against dimensionless bed height at the same set of operating conditions and are presented in Figure 3-10 and Figure 3-11 . It can be seen from these plots that the concentration of plastic is fairly evenly distributed throughout the riser. The coarse is very well-mixed with the fines. There is no accumulation of the coarse particles near the bottom of the bed as was seen by Hirschberg *et al* (1995). This difference can be explained in terms of particle terminal velocity, U_t.

The MIT cold model operates at a U_o of 2 m/s. It is expected that if U_t of particles is much smaller than U_o, particles can easily be entrained if the exit geometry does not limit particle entrainment. U_t can be calculated from the correlation:

$$U_t = \left[\frac{4gd_p(\rho_s - \rho_g)}{3\rho_g C_d} \right]^{1/2}$$

For plastic particles, the $d_p \sim 200$ μm and the U_t is calculated to be 0.162 m/s. Since U_o is more than 10 times the U_t of plastic, its even distribution along the entire riser can be explained.

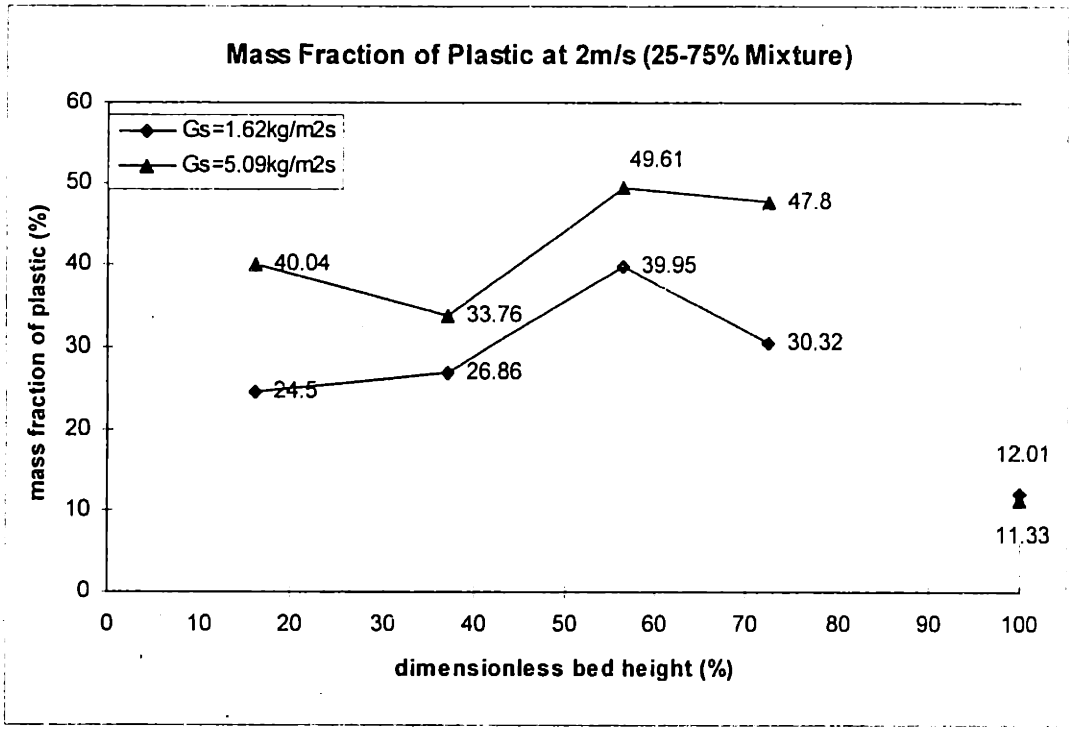

Figure 3-10 Mass Fraction of Plastic for a 25-75% Mixture at 2m/s

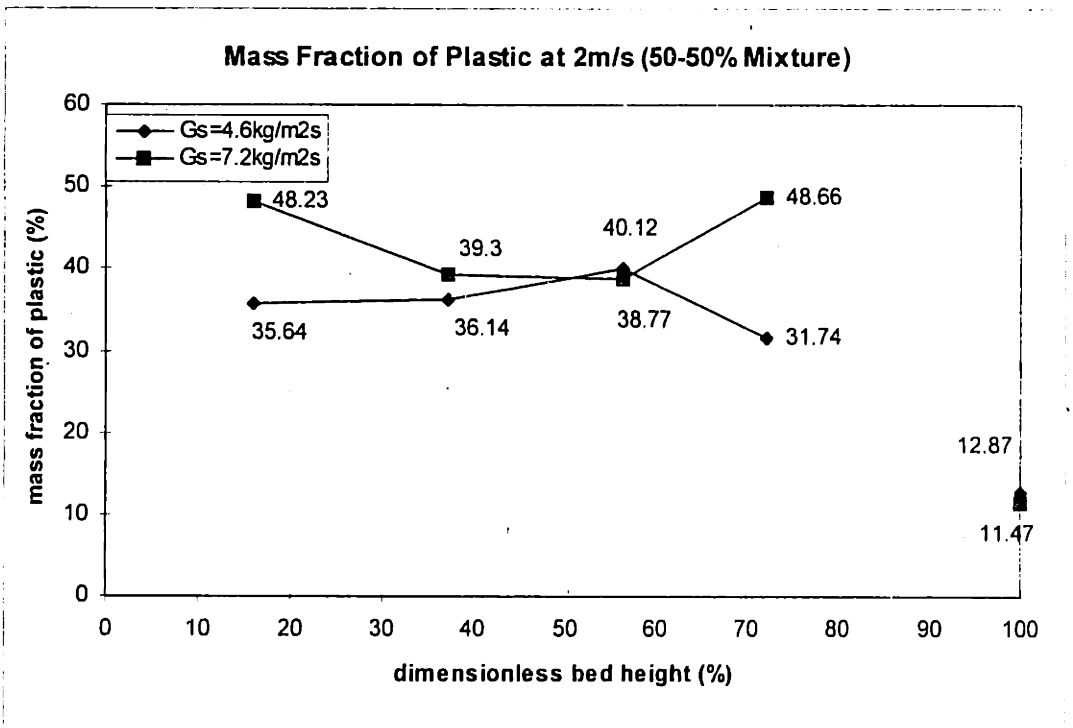

Figure 3-11 Mass Fraction of Plastic for a 50-50% Mixture at 2m/s

3.4.1 Mass Fraction of Coarse in the Annular Region for a 50-50% Mixture

While samples taken at the core region did not reflect sufficient coarse (plastic) particles at all levels of the riser (i.e. the mass fraction of plastic in the sample was less than the original mixture - 50%), samples taken in the annular region near the wall indicated a higher concentration of coarse particles.

An experiment was carried out to measure the mass fraction of plastic in the annular region near the wall near the bottom of the riser. The operating conditions are identical to the case with U_o= 2m/s, G_s= 7.2 kg/m^{2}s for a 50-50% mixture. The sample probe geometry is given by the following illustration.

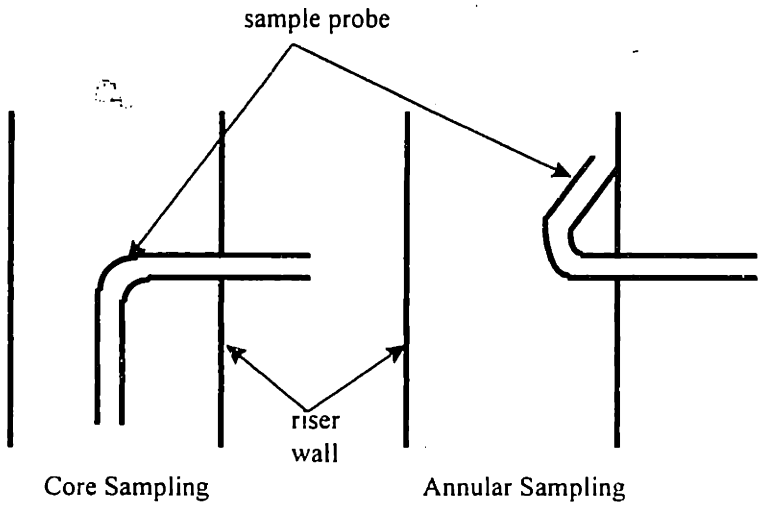

Figure 3-12 Core Sampling and Annular Sampling

Result indicated that at a dimensionless bed height of 16%, the mass fraction of plastic at the wall is 53.1%. At the same elevation in core sampling, the mass fraction of plastic was 48.2%. It can be seen that there is a 5% higher concentration of plastic by mass at the annular region as compared to the core region.

The radial velocity profile peaks at the center of the riser and decreases as it gets closer to the wall. With a low velocity near the wall, coarse particles have a tendency to leave the

core region for the wall. The low velocity near the wall has insufficient momentum to carry coarser and heavier particles upward. As a result, they fall and are recirculated again within the riser. The flow behavior in this model resembles that of the core-annular flow model. In addition, sample measurements at the exhaust of the primary cyclone indicated that most of the entrained particles are finer cork (about 89% of cork and 11% of plastic by mass). These entrained particles are re-injected into the riser and are transported mostly in the core to the exit at which point they leave the riser again. This suggests that majority of the plastic particles stay within the riser near the wall.

3.5 Particle Size Distribution

Particle size distribution study of sample is performed using a series mechanical sieves; and the mixture of sample with both plastic and cork were analyzed. Average diameter (ave d_p) for each sample port is calculated using the sauter mean definition as was given in Section 2.4.3. The results of PSD study are given in Figure 3-14 to Figure 3-17 .

It is observed that the ave d_p for the four sample ports in the riser are fairly evenly distributed (i.e. they range from approximately 145 to 210 microns) The mean particle diameter exiting the riser ranges from 90 to 147 microns. It is clear that more fines are exiting the riser. The fines follow the gas streamlines better than the coarse with the help of the abrupt geometry which gives rise to the inertial separation. These PSD results once again verify that the coarse and the fines in the riser are very well mixed.

In the annular down flow region, the average particle size is significantly larger than that found in the up flowing core. The PSD of sample collected at the bottom-most sample port (16% dimensionless bed height) for a 50-50% mixture is as follow. It has a mean d_p of 222 μm.

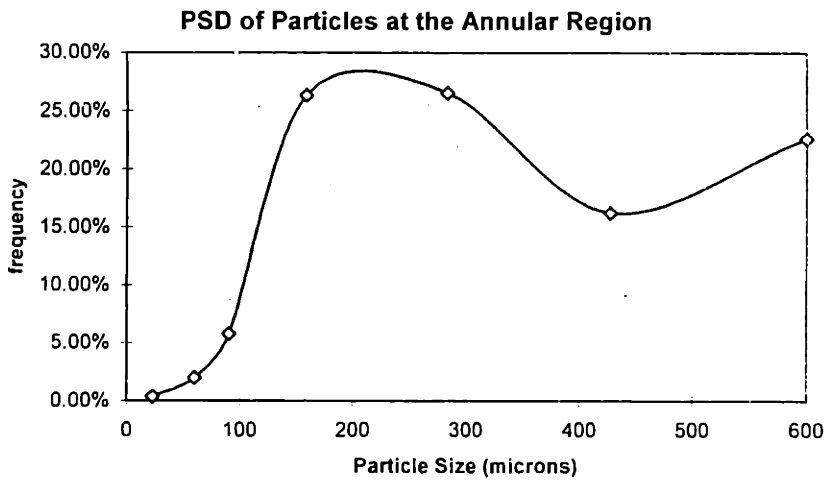

Figure 3-13 PSD of Samples Collected in the Annular Downflow Region (50-50% Mixture U_o=2 m/s G_s=7.2 kg/m^{2}s)

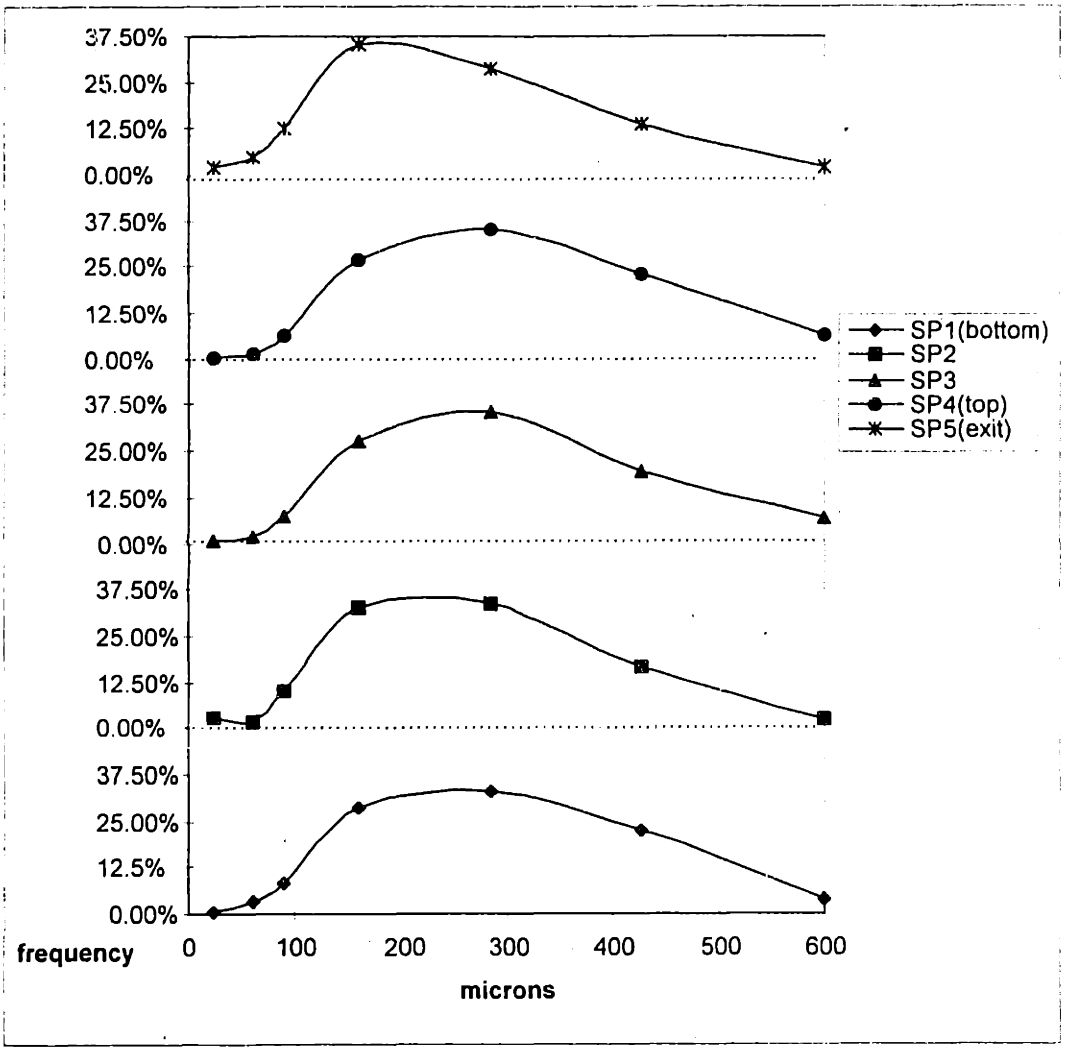

PSD - Range Frequency					
size (μm)	SP1(bottom)	SP2	SP3	SP4(top)	SP5
22.5	0.47%	2.86%	0.77%	0.37%	2.25%
60	3.39%	1.65%	2.21%	1.80%	4.80%
90.5	8.34%	10.16%	7.36%	6.69%	12.72%
159	28.40%	32.71%	27.98%	26.80%	35.32%
283.5	33.07%	33.79%	35.50%	35.09%	28.94%
427.5	22.70%	16.54%	19.46%	22.92%	13.89%
600	3.63%	2.29%	6.73%	6.34%	2.09%

ave d_p [μm]	191	158	196	210	147

Figure 3-14 [14] PSD of Samples Collected (25-75% Mixture U_o=2 m/s G_s=1.62 kg/m^{2}s)

[14] SP= Sample Port; SP1 is the bottom-most sample port in the riser and SP4 is the top-most. SP5 is the sample port located at the exit of the primary cyclone. "ave d_p" calculated for each sample port is the sauter mean particle diameter.

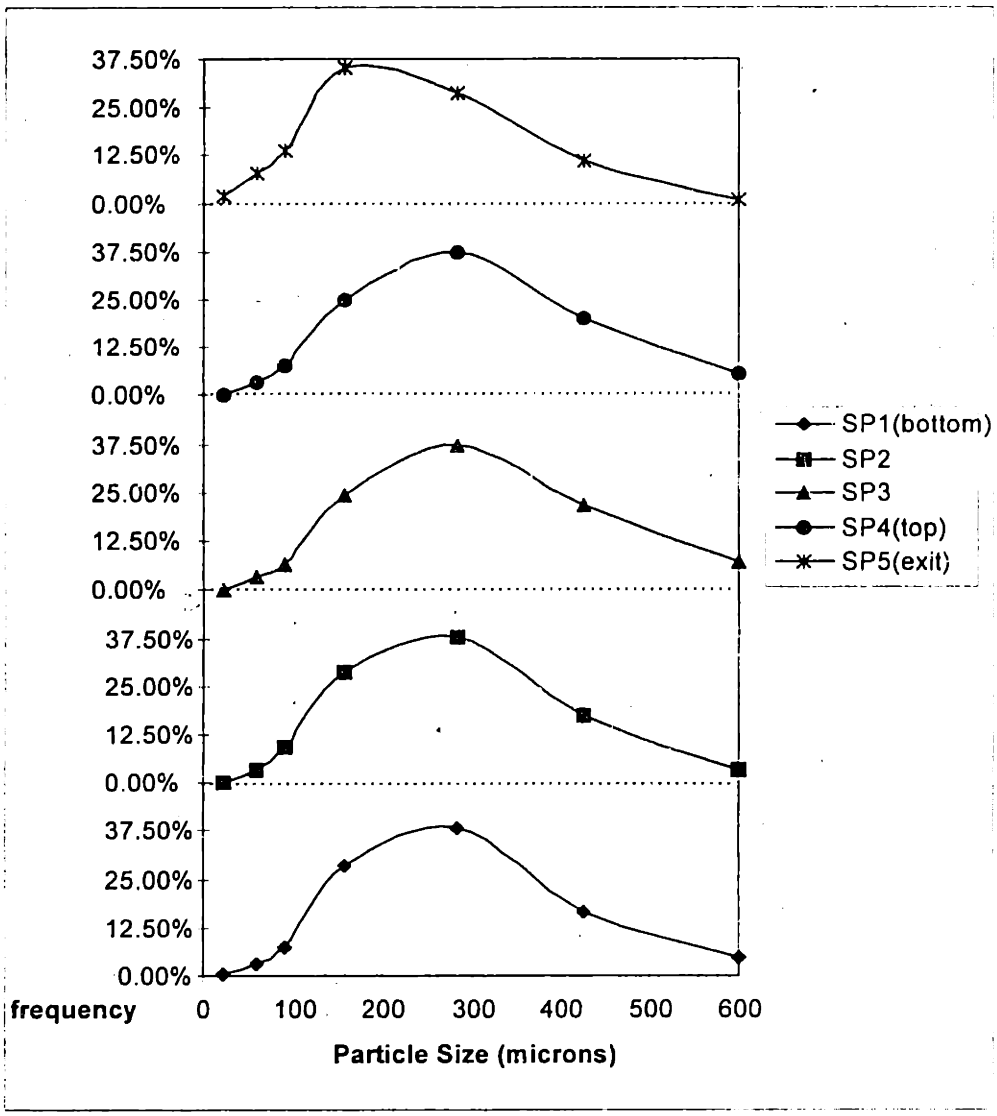

PSD - Range Frequency					
size (μm)	SP1(bottom)	SP2	SP3	SP4(top)	SP5
22.5	0.79%	0.00%	0.00%	0.36%	2.22%
60	3.45%	3.42%	3.17%	3.70%	8.11%
90.5	7.74%	9.29%	6.76%	7.62%	13.77%
159	28.36%	28.69%	24.14%	25.28%	35.51%
283.5	38.19%	37.98%	37.35%	37.59%	28.76%
427.5	16.72%	17.36%	21.55%	20.04%	10.96%
600	4.75%	3.26%	7.03%	5.41%	0.68%

ave d_p [μm]	186	192	211	196	136

Figure 3-15 PSD of Samples Collected (25-75% Mixture U_o=2 m/s G_s=5.75 kg/m^{2}s)

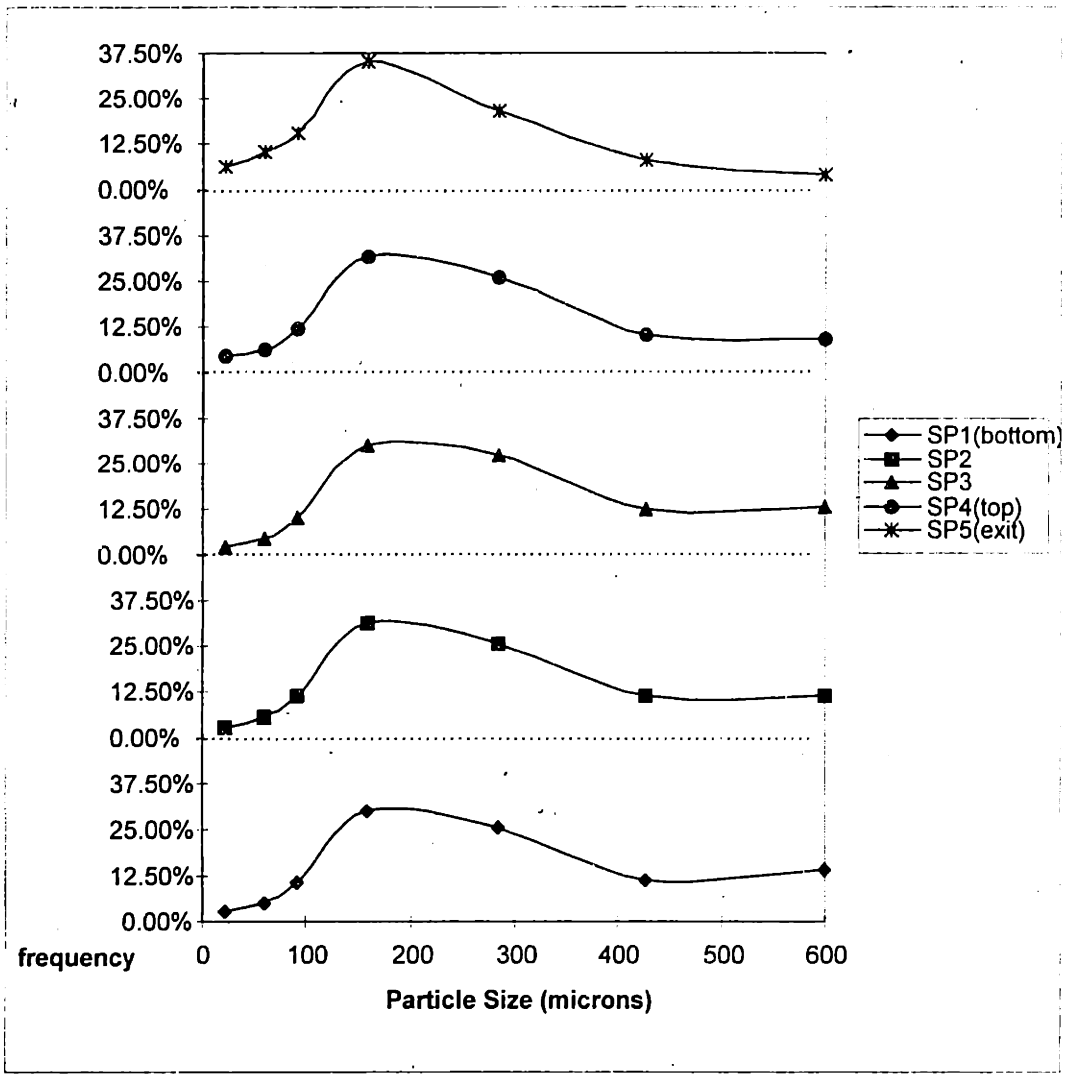

PSD - Range Frequency					
Size (µm)	SP1(bottom)	SP2	SP3	SP4(top)	SP5
22.5	2.89%	2.84%	2.02%	4.65%	6.08%
60	5.34%	5.94%	4.80%	6.07%	10.36%
90.5	11.05%	11.53%	10.45%	12.21%	15.36%
159	29.92%	31.48%	30.19%	31.66%	35.06%
283.5	25.29%	25.33%	27.21%	26.14%	21.49%
427.5	11.20%	11.38%	12.43%	10.06%	7.73%
600	14.30%	11.50%	12.89%	9.20%	3.92%

ave d_p [µm]	150	146	161	129	107

Figure 3-16 PSD of Samples Collected (50-50% Mixture U_o=2 m/s G_s=4.6 kg/m^{2}s)

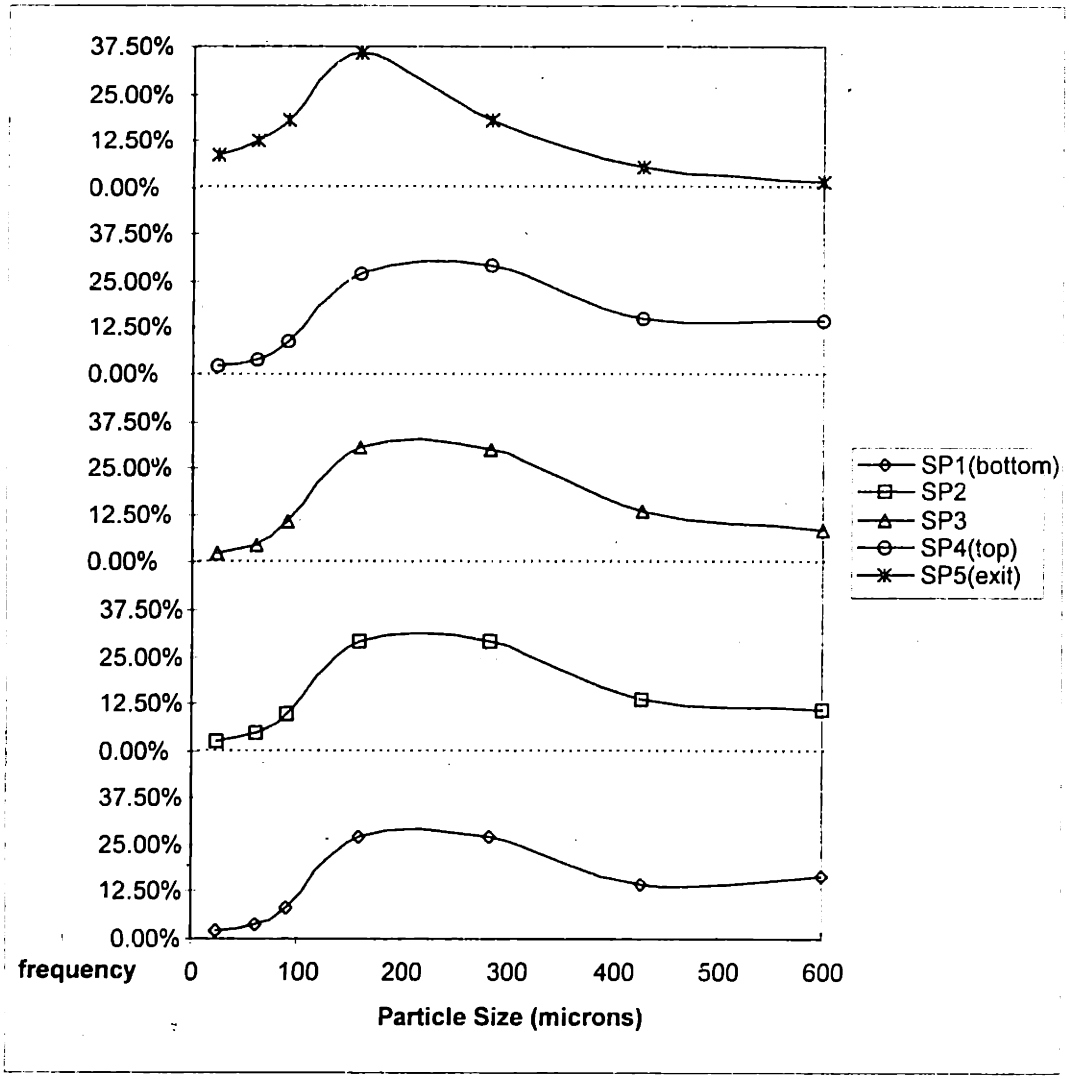

PSD - Range Frequency					
size (μm)	SP1(bottom)	SP2	SP3	SP4(top)	SP5
22.5	2.18%	2.47%	2.48%	1.98%	8.98%
60	3.86%	4.94%	4.69%	3.76%	12.44%
90.5	8.30%	9.61%	10.45%	9.08%	18.23%
159	27.05%	29.01%	30.46%	26.95%	35.89%
283.5	27.28%	29.33%	30.05%	29.10%	17.87%
427.5	14.57%	13.47%	13.43%	14.84%	5.15%
600	16.75%	11.16%	8.44%	14.28%	1.44%

ave d_p [μm]	172	158	155	172	90

Figure 3-17 PSD of Samples Collected (50-50% Mixture U_0=2 m/s G_s=7.2 kg/m^{2}s)

4. Conclusion

The pyrolyzer with its current geometry effectively acts as a particle separator. Particles are well mixed within the riser due to the high superficial gas velocity as can be seen by the uniform distribution of the plastic (coarse) and cork (fine) from the sample concentration and PSD study. The abrupt exit gives rise to a higher level of particle reflection due to inertia separation, enabling a higher portion of heavier plastic particles to be recirculated within the riser. Cork on the other hand, follows the gas streamline better relative to the plastic and thus has a higher tendency to exit the riser.

For both the 25-75% and the 50-50% mixtures, an increase in solid recirculation rate results in an increase in the overall solid concentration in the riser. For the 25-75% mixture, there is a relatively sharp increase in solid concentration near the exit of the riser regardless of the flux. Due to the exit geometry, most of the plastic particles introduced into the riser are being retained. These particles have a strong presence near the core region of the riser as was seen in the sample measurements. For the 50-50% mixture, the overall solid concentration throughout riser becomes more uniform as the flux increases, as can be seen by the more uniformly distributed solid profile. There is still a high plastic concentration within the riser since only a small fraction of plastic exit the riser. Sample measurement near the riser wall at the annular downflow region indicated that there is a high concentration of coarser plastic particles in this region as compared to the core region of the riser.

This series of experiments provides a first insight and a reasonable understanding of the hydrodynamics of the pyrolyzer. Improvements on our current experimental technique can be made. For instance, a better sample analysis technique can predict more precisely the material composition for a given sample by measuring its true solid density rather than its bulk density. However, more sophisticated equipment such as a helium pycnometer may be necessary for such improvements.

REFERENCES

Beckwith, Marangoni and Lienhard, "Mechanical measurements", 5th edition. Addison Wesley Publishing Co. (1993)

Brereton, C and Grace J.R., "End effects in circulating fluidized bed hydrodynamics", *Circulating Fluidized Bed Technology IV, AIChE*, P. 137-144. (1994)

Davidson, J.F., Clift. R., and Harrison, D., "Fluidization", 2nd edition. Academic Press. (1985)

Davies, J.T., "Turbulence phenomena", Academic Press, Inc. (1972)

Farrell, P., "Hydrodynamic scaling and solids mixing in pressurized bubbling fluidized bed combustors", *Massachusetts Institute of Technology doctoral thesis.* (1996)

Glicksman, L.R., "Scaling relationships for fluidized beds", *Chem. Engng Sci.* 39, No 9, 1373-1379. (1984)

Glicksman, L.R., "Scaling relationships for fluidized beds", *Chem. Engng Sci.* 43, 1419-1421. (1988)

Glicksman, L.R., Hyre, M., and Woloshun, K., "Simplified scaling relationships for fluidized beds", *Powder Tech.* 77, 177-199. (1993)

Glicksman, L.R., Hyre, M.R., and Farrell, P.A., "Dynamic similarity in fluidization", *Int. J Multiphase Flow* 20, 331-386. (1994)

Glicksman, L.R., Farrell, P.A., and Hyre, M.R., "Verification of a simplified set of hydrodynamic scaling relationships for pressurized fluidized bed combustors", preprints of AIChe 1995 annual meeting, Maimi Beach, FL. Nov 12-17, 95. P 117-121

Herb, B., Dou, S., Tuzla, K., and Chen, J.C., "Solid mass fluxes in circulating fluidized beds", *Powder Technology* 70, 197-205. (1992)

Hirschberg, B., Werther, J., Delebarre, A., and Koniuta, A., "Mixing and segregation of solids in a circulating fluidized bed", *Fluidization VIII,* 281-290. (1995)

Hyre, M.R., "Aspects of hydrodynamics and heat transfer in circulating fluidized beds", *Massachusetts Institute of Technology doctoral thesis.* (1995)

Kunii, D., and Levenspiel, O., "Fluidization engineering", 1st edition. Robert E. Krieger Publishing Company. (1969)

Miller, R.W., "Flow measurement engineering handbook", McGraw-Hill. (1983)

Weast, R.C., "Handbook of chemistry and physics", 57th edition. CRC Press. (1977)

Wen, C.Y., and Yu, Y.H., *AIChe Journal,* 12, 610 (1966)

Westphalen, D., "Experimental verification of scaling relationships for circulating fluidized beds", *Massachusetts Institute of Technology Master thesis.* (1990)

Appendix A - Material Density Estimation of Spent Sorbent

Established material densities (particle void fraction, $\varepsilon = 0$)

ρ_{CaCO3} = 2.75 g/ml (172 pcf)
ρ_{CaO} = 3.25 - 3.38 g/ml (206 pcf)
ρ_{CaS} = 2.5 g/ml (156 pcf)

Measured material densities:

ρ_{CaCO3} = 2.75 g/ml (172 pcf)

ρ_{CaO} = 2.75 g/ml (172 pcf) $\Rightarrow$ particle void fraction, $\varepsilon = 1 - \frac{2.75}{3.3} = 0.167$

Estimated material density

ρ_{CaS} : assuming a particle void fraction, $\varepsilon = 0.167$, $\rho_{CaS} = (1 - 0.167)(2.5 \text{ g/ml})$ = 2.1 g/ml (131 pcf)

Estimated material density of spent sorbent

Chemical composition of spent sorbent $\approx$ 50% CaO, 50% CaS
$\rho_{\text{spent sorbent}} = .5\rho_{CaO} + .5\rho_{CaS} = .5\,(2.75 + 2.1) =$ 2.43 g/ml (152 pcf)

Spent sorbent density measurement

Char and spent sorbent mixture has been separated by using the 'floater - sinker' method. Char is the floater and spent sorbent is the sinker. The two separated materials were then collected and air dried. Density measurement of spent sorbent using oil displacement method was taken.

mass of spent sorbent	$\equiv$	2.731 g
volume of oil displaced	$\approx$	1.3 ml

$\rho_{\text{spent sorbent}}$ = 2.1 g/ml (130 pcf)

From the estimated and measured densities, the range of $\rho_{\text{spent sorbent}}$ is approximately 2.1 - 2.4 g/ml

Appendix B - Summary of Possible Cold Model Particles Simulating Char

Material	Vendor	Description
Wood flour	1. American Wood Fibers 2. Beede, Louis & Sons. (508) 452 8906	density, $\rho \approx 15$ pcf = .24 g/cc max. particle dia. dp $\approx$ 120 μm (mesh 140) Individual particle in cylindrical form and is fiberous. With a typical aspect ratio of 4 - 8. The geometry does not suggest this to be an ideal material to simulate char.
Granulated cork wood	1. Expanko Cork (800) 662 2675 2. Maryland Cork Co. (410) 398 2955*	Density $\approx$ .24 g/cc. Particles are available in a wide range of sizes; Down from around 15 microns to about 500 microns. Produced by grinding operation.
Hollow glass spheres	1. 3M (612) 737 1751 (612) 736 2774 2. PQ Corp. (615) 629 7160	3M Type 1 (K15) density = .15 g/cc dp(10) = 35μm, dp(50) = 68μm, dp(90) = 106 μm Type 2 (K20) density = .20 g/cc dp(10) = 31μm, dp(50) = 59μm, dp(90) = 88 μm PQ Corp. Type 1 (Qcel2106) density = .20 g/cc mean dp = 85μm ranges from 5-180μm Type 2 (Qcel2116) density = .13 g/cc mean dp = 89μm ranges from 5-200μm

* Granulated Cork was purchased from Maryland Cork Co.

Appendix C - Experimental Measurement of Mass Fraction of Plastic and Mixture Bulk Density

All mass measurements have units [g] while volume measurements are in [cm^3]
Unit for density [g/cm^3]
"Desired M (cork)" is the mass of cork that should be mixed with the given mass of plastic mixture.
"Desired M (total)" is the total mass of the mixture that should be obtained after cork is mixed with the plastic.

CALIBRATION CURVE I

set 1								Density		
Controled M(plastic) %	M(plastic)	Desired M(total)	Desired M(cork)	Actual M(cork)	M(total)	M % cork	M % plastic	mass meas.	volume	density
100%	1.7	1.70	0.00	0	1.7	0.00%	100.00%	1.7	3.55	0.479
90%	0.6	0.67	0.07	0.06	0.66	9.09%	90.91%	0.66	1.5	0.440
80%	0.73	0.91	0.18	0.2	0.93	21.51%	78.49%	0.92	2.2	0.418
70%	0.64	0.91	0.27	0.27	0.91	29.67%	70.33%	0.9	2.15	0.419
60%	0.61	1.02	0.41	0.42	1.03	40.78%	59.22%	1.03	2.7	0.381
50%	0.68	1.36	0.68	0.67	1.35	49.63%	50.37%	1.36	3.6	0.378
40%	0.48	1.20	0.72	0.81	1.29	62.79%	37.21%	1.3	3.6	0.361
30%	0.5	1.67	1.17	1.17	1.67	70.06%	29.94%	1.67	4.9	0.341
20%	0.5	2.50	2.00	2.02	2.52	80.16%	19.84%	2.5	7.3	0.342
10%	0.23	2.30	2.07	2.07	2.3	90.00%	10.00%	2.3	7.15	0.322
0%	0			0.85	0.85	100.00%	0.00%	0.85	2.8	0.304

set 2								Density		density
Controled M(plastic) %	M(plastic)	Desired M(total)	Desired M(cork)	Actual M(cork)	M(total)	M % cork	M % plastic	mass meas.	volume	
100%	1.22	1.22	0.00	0	1.22	0.00%	100.00%	1.22	2.6	0.469
90%	0.73	0.81	0.08	0.1	0.83	12.05%	87.95%	0.84	1.9	0.442
80%	0.8	1.00	0.20	0.2	1	20.00%	80.00%	1.02	2.35	0.434
70%	0.72	1.03	0.31	0.32	1.04	30.77%	69.23%	1.05	2.6	0.404
60%	0.62	1.03	0.41	0.41	1.03	39.81%	60.19%	1.02	2.7	0.378
50%	0.73	1.46	0.73	0.73	1.46	50.00%	50.00%	1.48	3.95	0.375
40%	0.7	1.75	1.05	1.05	1.75	60.00%	40.00%	1.75	4.9	0.357
30%	0.72	2.40	1.68	1.68	2.4	70.00%	30.00%	2.4	7.5	0.320
20%	0.33	1.65	1.32	1.33	1.66	80.12%	19.88%	1.66	5.1	0.325
10%	0.245	2.45	2.21	2.23	2.475	90.10%	9.90%	2.49	8.25	0.302
0%	0			0.97		100.00%	0.00%	0.97	3.5	0.277

set 3								Density		
Controled M(plastic) %	M(plastic)	Desired M(total)	Desired M(cork)	Actual M(cork)	M(total)	M % cork	M % plastic	mass meas.	volume	density
100%	2.22	2.22	0.00	0	2.22	0.00%	100.00%	2.22	4.6	0.483
90%	2.07	2.30	0.23	0.25	2.32	10.78%	89.22%	2.34	5.1	0.459
80%	1.32	1.65	0.33	0.33	1.65	20.00%	80.00%	1.64	3.8	0.432
70%	1.16	1.66	0.50	0.5	1.66	30.12%	69.88%	1.66	4	0.415
60%	1.18	1.97	0.79	0.8	1.98	40.40%	59.60%	1.99	5	0.398
50%	1.06	2.12	1.06	1.06	2.12	50.00%	50.00%	2.13	5.55	0.384
40%	1.09	2.73	1.64	1.68	2.77	60.65%	39.35%	2.77	7.55	0.367
30%	0.79	2.63	1.84	1.85	2.64	70.08%	29.92%	2.63	8	0.329
20%	0.56	2.80	2.24	2.3	2.86	80.42%	19.58%	2.88	8.8	0.327
10%	0.245	2.45	2.21	2.23	2.475	90.10%	9.90%	2.49	8.25	0.302
0%	0			2.09		100.00%	0.00%	2.1	7.5	0.280

CALIBRATION CURVE II

set 1						Density		
Controled M(plastic) %	M(plastic)	M(cork)	M(total)	M % cork	M % plastic	mass meas.	volume	density
100%	2.04	0	2.04	0.00%	100.00%	2.04	4.5	0.453
80%	0.73	0.2	0.93	21.51%	78.49%	0.94	2.4	0.392
60%	0.61	0.41	1.02	40.20%	59.80%	0.98	2.6	0.377
40%	0.48	0.72	1.2	60.00%	40.00%	1.26	3.8	0.332
20%	0.5	2	2.5	80.00%	20.00%	1.23	5.7	0.216

set 2						Density		
Controled M(plastic) %	M(plastic)	M(cork)	M(total)	M % cork	M % plastic	mass meas.	volume	density
100%	1.22	0	1.22	0.00%	100.00%	1.46	3.2	0.456
80%	0.8	0.22	1.02	21.57%	78.43%	1.01	2.7	0.374
60%	0.62	0.44	1.06	41.51%	58.49%	1.07	3	0.357
40%	0.7	1.04	1.74	59.77%	40.23%	1.75	5.2	0.337
20%	0.33	1.32	1.65	80.00%	20.00%	1.73	5.5	0.315

set 3						Density		
Controled M(plastic) %	M(plastic)	M(cork)	M(total)	M % cork	M % plastic	mass meas.	volume	density
100%	2.22	0.00	2.22	0.00%	100.00%	1.89	4.1	0.461
80%	1.32	0.33	1.65	20.00%	80.00%	1.67	4.1	0.407
60%	1.18	0.79	1.97	40.00%	60.00%	1.94	4.9	0.396
40%	1.09	1.64	2.73	60.00%	40.00%	1.67	5.5	0.304
20%	0.56	2.24	2.80	80.00%	20.00%	0.8	2.9	0.276

Appendix D - Pressure Transducers Calibrations

Summary of pressure transducer calibration curves:

PRSSURE TRANSDUCER CHANNEL, LOCATION AND CALIBRATION					
easytx					
Channel	Transducer	Calibration Curve	Range Valid	Sensitivity Description	Location
0	1204998	P = 2.51V - 2.75	1 - 5 V	10" of wc	Riser lowest
1	1205000	P = 2.52 V - 2.77	1 - 5 V	10" of wc	
2	1204999	P = 2.5 V - 2.7	1 - 5 V	10" of wc	in between riser
3	1205001	P = 1.23 V - 1.39	1 - 5 V	5" of wc	
4	1204977	P = 1.24 V - 1.36	1 - 5 V	5" of wc	
5	1204978	P = 1.25 V - 1.3	1 - 5 V	5" of wc	Riser highest
		P [in of wc], V [V]			

Calibration for Pressure Transducer 1 (channel 0)

calibration curve: P = 2.51 V - 2.75 variance: 3.25e-4

Pressure Transducer Calibration			
Pressure transducer 1 (channel 0)			
mano. reading		voltage	del. P
(" water)		(V)	(" water)
0.11		1.1004	0
0.94		1.4305	0.83
3.4		2.3994	3.29
3.7		2.524915	3.59
6.5		3.64	6.39
8.8		4.57134	8.69
9.8		4.954395	9.69

Calibration for Pressure Transducer 2 (channel 1)

calibration curve: P = 2.52 V - 2.77 variance: 4.94e-5

Pressure Transducer Calibration			
Pressure transducer 2 (channel 1)			
mano. reading		voltage	del. P
(" water)		(V)	(" water)
0.1		1.104	0
0.39		1.22	0.29
1.4		1.617	1.3
4.05		2.669	3.95
9.2		4.72	9.1

Calibration for Pressure Transducer 3 (channel 2)

calibration curve: P = 2.5 V - 2.7 variance: 5.00e-4

Pressure Transducer Calibration			
Pressure transducer 3 (channel 2)			
mano. reading		voltage	del. P
(" water)		(V)	(" water)
0.15		1.0804	0
0.62		1.274	0.47
2.3		1.9304	2.15
5.3		3.122	5.15
8.8		4.539	8.65
9.9		4.973	9.75

Calibration for Pressure Transducer 4 (channel 3)

calibration curve: P = 1.23 V - 1.39 variance: 4.09e-4

Pressure Transducer Calibration			
Pressure transducer 4 (channel 3)			
mano. reading		voltage	del. P
(" water)		(V)	(" water)
0.15		1.1397	0
0.9		1.7347	0.75
1.9		2.524	1.75
3.5		3.852	3.35
4.8		4.91	4.65

Calibration for Pressure Transducer 5 (channel 4)

calibration curve: P = 1.24 V - 1.36 variance: 1.75e-4

Pressure Transducer Calibration			
Pressure transducer 5 (channel 4)			
mano. reading		voltage	del. P
(" water)		(V)	(" water)
0.15		1.1063	0
0.87		1.682	0.72
1.6		2.254	1.45
2.9		3.3227	2.75
4.6		4.698	4.45

Calibration for Pressure Transducer 6 (channel 5)

calibration curve: P = 1.25 V - 1.3 variance: 5.26e-4

Pressure Transducer Calibration			
Pressure transducer 6 (channel 5)			
mano. reading		voltage	del. P
(" water)		(V)	(" water)
0.15		1.0494	0
0.985		1.7127	0.835
1.95		2.4587	1.8
3.8		3.946	3.65
4.9		4.856	4.75